Shallow and Deep Eastern Boundary Currents in the South Atlantic at 34.5°S: Mean Structure and Variability

Marion Kersalé, Renellys C. Perez, Sabrina Speich, Christopher S. Meinen, Tarron Lamont, Matthieu Le Hénaff, Marcel A. van den Berg, Sudip Majumder, Isabelle J. Ansorge, Shenfu Dong, et al.

▶ **To cite this version:**

Marion Kersalé, Renellys C. Perez, Sabrina Speich, Christopher S. Meinen, Tarron Lamont, et al.. Shallow and Deep Eastern Boundary Currents in the South Atlantic at 34.5°S: Mean Structure and Variability. Journal of Geophysical Research. Oceans, 2019, 124, pp.1634-1659. 10.1029/2018JC014554 . insu-03683206

HAL Id: insu-03683206
https://insu.hal.science/insu-03683206

Submitted on 1 Jun 2022

HAL is a multi-disciplinary open access archive for the deposit and dissemination of scientific research documents, whether they are published or not. The documents may come from teaching and research institutions in France or abroad, or from public or private research centers.

L'archive ouverte pluridisciplinaire **HAL**, est destinée au dépôt et à la diffusion de documents scientifiques de niveau recherche, publiés ou non, émanant des établissements d'enseignement et de recherche français ou étrangers, des laboratoires publics ou privés.

Copyright

JGR Oceans

RESEARCH ARTICLE
10.1029/2018JC014554

Shallow and Deep Eastern Boundary Currents in the South Atlantic at 34.5°S: Mean Structure and Variability

Marion Kersalé[1,2], Renellys C. Perez[2], Sabrina Speich[3], Christopher S. Meinen[2], Tarron Lamont[4,5], Matthieu Le Hénaff[1,2], Marcel A. van den Berg[5], Sudip Majumder[1,2], Isabelle J. Ansorge[4], Shenfu Dong[2], Claudia Schmid[2], Thierry Terre[6], and Silvia L. Garzoli[1,2]

[1]Cooperative Institute for Marine and Atmospheric Studies, University of Miami, Miami, FL, USA, [2]NOAA/Atlantic Oceanographic and Meteorological Laboratory, Miami, FL, USA, [3]Laboratoire de Météorologie Dynamique, UMR 8539 École Polytechnique, ENS, CNRS, Paris, France, [4]Marine Research Institute, Department of Oceanography, University of Cape Town, Rondebosch, South Africa, [5]Department of Environmental Affairs, Oceans and Coastal Research, Cape Town, South Africa, [6]IFREMER, University Brest, CNRS, IRD, Laboratoire d'Océanographie Physique et Spatiale (LOPS), IUEM, Plouzané, France

Key Points:
- Velocity and water mass observations demonstrate the presence of two distinct eastern boundary currents
- Volume transport fluctuations of the two boundary currents are strongest at period of 30-90 days
- Much of the deep eastern boundary current must be recirculating in the basin rather than participating in the overturning circulation

Correspondence to:
M. Kersalé,
marion.kersale@noaa.gov

Citation:
Kersalé, M., Perez, R. C., Speich, S., Meinen, C. S., Lamont, T., Le Hénaff, M., et al. (2019). Shallow and deep eastern boundary currents in the South Atlantic at 34.5°S: Mean structure and variability. *Journal of Geophysical Research: Oceans*, *124*, 1634–1659. https://doi.org/10.1029/2018JC014554

Received 11 SEP 2018
Accepted 23 JAN 2019
Accepted article online 28 JAN 2019
Published online 14 MAR 2019

Abstract The first in situ continuous full-water-column observations of the eastern boundary currents (EBCs) at 34.5°S in the South Atlantic are obtained using 23 months of data from a line of Current and Pressure recording Inverted Echo Sounders (CPIES) spanning the Cape Basin. The CPIES are used to evaluate the mean structure of the EBC, the associated water masses, and the volume transport variability. The estimated northward time-mean Benguela Current absolute geostrophic transport is 24 Sv, with a temporal standard deviation of 17 Sv. Beneath this current the time-mean transport is southward, indicating the presence of a deep-EBC (DEBC), with a time-mean transport of 12 Sv, and a standard deviation of 17 Sv. Offshore of these currents, the shallow and deep flows are more variable with weak time means, likely influenced by Agulhas Rings transiting through the region. Hydrographic data collected along the CPIES line demonstrate that the DEBC is carrying recently ventilated North Atlantic Deep Water, as it flows along the continental slope. This is consistent with a previously hypothesized interior pathway bringing recently ventilated North Atlantic Deep Water from the Deep Western Boundary Current across the Atlantic to the Cape Basin. The observations further indicate that much of the DEBC must recirculate within the basin. Spectral analyses of the shallow and deep EBC transport time series demonstrate that the strongest variability occurs on timescales ranging from 30 to 90 days, associated with the propagation of Agulhas Rings.

Plain Language Summary Heat and freshwater transported by the overturning circulation in the Atlantic have been shown to have significant influences on global climate. Boundary current variations in the Southeast Atlantic have furthermore been shown to play a major role in the overturning circulation. This study presents, for the first time, full-depth, daily observations of the eastern boundary currents at 34.5°S based on moored instruments. The 23 months of observations (velocity and water mass properties) reveal the presence of two distinct eastern boundary currents, with equatorward flow in the upper layer and poleward flow in the deep layer. The variability of both currents is characterized, in unprecedented detail, and is shown to be dominated by large anticyclonic eddies transiting across the moorings. The observations further indicate that much of the deep current must recirculate within the Cape Basin, with a smaller portion of the flow participating in the global overturning circulation.

1. Introduction

The meridional overturning circulation (MOC) is a variable-in-time three-dimensional circulation system centered in the Atlantic Ocean but encompassing all of the ocean basins (e.g., Gordon, 1986; Lumpkin & Speer, 2007; Talley, 2003). The MOC carries the majority of the oceanic components of the global transport of mass, heat, and salt, and it thus has profound impacts on regional and global climate (e.g., Rahmstorf et al., 2015). The Atlantic pathways followed by the MOC flows are complex, sometimes carried within strong tightly confined boundary currents and at other times forging alternate routes (e.g., Lozier, 2010; Stommel, 1957). Both zonal and meridional flows play significant roles in the global MOC, and transport

©2019. American Geophysical Union. All Rights Reserved.

by eddies in some locations is considered crucial (Bower et al., 2009; Dengler et al., 2004; Garzoli et al., 2015; van Sebille et al., 2012). Nevertheless, in its simplest "conveyor-belt" form, the MOC in the Atlantic can be thought of as originating by the sinking of newly ventilated North Atlantic Deep Water (NADW) in the high-latitude North Atlantic, followed by the southward spreading of this NADW through the Atlantic basin to the Southern Ocean, slow upward mixing around the globe, and the return of warm/salty thermocline and surface waters through the Atlantic basin to close this loop (e.g., Bingham et al., 2007; Buckley & Marshall, 2016; Gordon, 1986; Perez et al., 2015). One overall effect of these circulations in the South Atlantic is a net equatorward heat flux, making the South Atlantic unique among the other basins (e.g., Garzoli & Baringer, 2007; Talley, 2003). Several numerical model studies have suggested that the MOC variability can originate and/or be controlled in the South Atlantic via water masses mixing and via interbasin exchanges of heat and, in particular, via salt transport at 34.5°S (Biastoch et al., 2008; Dijkstra, 2007; Dong et al., 2011; Drijfhout et al., 2011; Gordon et al., 1992; Huisman et al., 2010; Weijer et al., 1999). Thus, the South Atlantic's role in the MOC must be better quantified through in situ measurements.

Moored arrays have been deployed at several locations as part of an international initiative to study the South Atlantic MOC (Ansorge et al., 2014; Garzoli & Matano, 2011; Hummels et al., 2015; Kopte et al., 2017; Meinen et al., 2013, 2017, 2018). One of the main components of this initiative is the South Atlantic MOC Basin-wide Array (SAMBA; Figure 1a) that has been under development along 34.5°S since 2008–2009. The SAMBA array was designed to capture the transport associated with the western boundary currents and eastern boundary currents (EBC) as well as the interior flows via estimation of geostrophic transports (Ansorge et al., 2014; Meinen et al., 2013, 2018; Perez et al., 2011). The choice of 34.5°S for the array was based on analyses indicating that latitude was crucial for evaluating MOC variability and the impact of interocean exchanges (e.g., Schiermeier, 2013). Moreover, this latitude was found to be well suited to observe the MOC with geostrophic velocity measurement systems along the boundaries (Goes et al., 2015; Perez et al., 2011). Another advantage of 34.5°S is that other MOC estimates exist at that latitude, from repeated transbasin expendable bathythermograph (XBT) observations (Dong et al., 2009; Garzoli et al., 2013), Argo (Dong et al., 2014), Argo/altimetry syntheses (Dong et al., 2015; Majumder et al., 2016), and sea surface temperature proxies (Lopez et al., 2017), which enable further comparisons.

The two main paths of the upper limb of the MOC entering into the South Atlantic (Figure 1a, yellow arrows) have been well documented as the cold water route through the Drake Passage (e.g., Chereskin et al., 2009; Donohue et al., 2016; Rintoul, 1991) and the warm water route coming from the Indian Ocean via the Agulhas Current System (e.g., Ansorge et al., 2005; Gladyshev et al., 2008; Gordon et al., 1992; Speich et al., 2007). The cold water route involves Antarctic Intermediate Water (AAIW) imported from the southeast Pacific through Drake Passage (e.g., Rintoul, 1991). The warm water route is characterized by the transport of warmer and saltier thermocline Indian Ocean waters into the Atlantic Ocean through the Cape Basin, via the Agulhas leakage (e.g., de Ruijter et al., 1999; Gordon et al., 1992; Lutjeharms, 2006; Lutjeharms & Cooper, 1996). The distinction between cold and warm route is somewhat artificial, however, as some studies have shown that there is a cold and fresh contribution of AAIW from the Indian Ocean to the Atlantic Ocean via the Agulhas leakage that takes part in the warm route (Gordon et al., 1992; Rusciano et al., 2012; Speich et al., 2007). Regardless of that nuance, studies based on numerical simulations have shown that waters from both the cold and warm water routes pass through the Cape Basin region west of South Africa, interacting with and/or merging with the Benguela Current as it flows northwestward (Figure 1a; e.g., Schmid et al., 2000; Speich, Blanke, & Cai, 2007; Rimaud et al., 2012; Rusciano et al., 2012).

The lower limb of the MOC in the South Atlantic (Figure 1a, blue arrows), which primarily transports recently ventilated NADW, has traditionally been thought to be carried predominantly by the Deep Western Boundary Current (DWBC) along much of the latitudinal breadth of the South Atlantic (e.g., Garzoli et al., 2015). Recently ventilated NADW is generally characterized by dissolved oxygen concentrations larger than 5.2 ml/L or 240 micromol/kg along the western boundary (Figure 1b; Garzoli et al., 2015; Herrford et al., 2017; Koltermann et al., 2011; Meinen et al., 2017; Valla et al., 2018). Previous experiments with moored instruments have shown that the DWBC is coherent and attached to the South American continental slope from the equator until roughly 8°S, where it appears to break up into a chain of eddies flowing southward along the boundary (Dengler et al., 2004; Herrford et al., 2017; Hummels

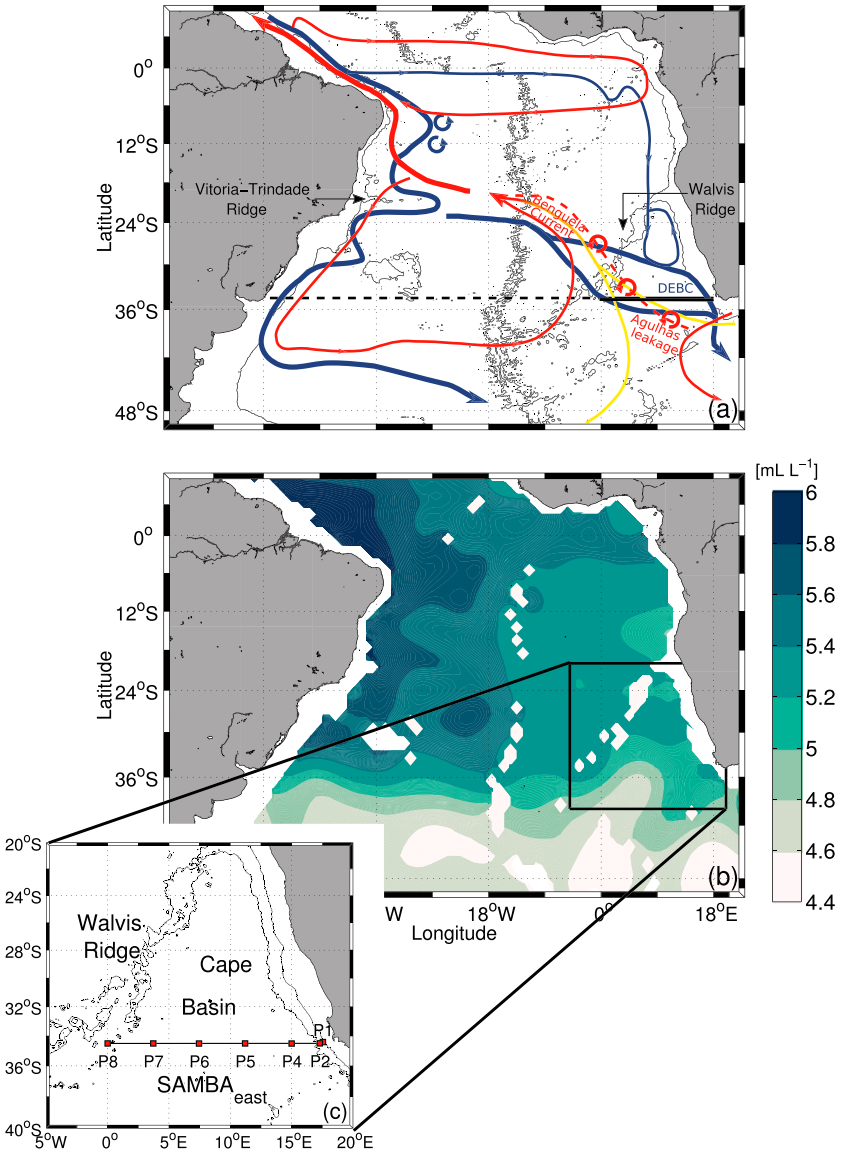

Figure 1. (a) Schematic circulation of the upper/intermediate meridional overturning circulation (MOC) limb is shown with red/yellow arrows, and the lower MOC limb in blue (Arhan et al., 2003; Lumpkin & Speer, 2007; Speich et al., 2007). The thick black line denotes the position of the full South Atlantic MOC Basin-wide Array (SAMBA) transect, with the solid black line denoting its eastern component, SAMBA-East, which is at the focus of the present study. The thin black contours characterize the 3,000-m isobath. (b) Study area with shaded color representing the oxygen concentrations (ml/L) at 3,000 m from the World Ocean Atlas annual climatology. (c) Horizontal positions of the current and pressure recording inverted echo sounders identified by the red squares along the SAMBA-East transect. The black contours characterize the 1,000- and 3,000-m isobaths. The topography in (a) and (c) comes from the Smith and Sandwell (1997) database with a horizontal resolution of 30 arc seconds.

et al., 2015; Schott et al., 2005). This deep flow of eddies continues along the continental shelf of South America until about 20°S, where the flow reaches the Vitória-Trindade Ridge (Figure 1a), which extend eastward from the South American shelf. At this point the flow carried by the eddy-chain appears to split into a component that continues along the western boundary and a component that flows zonally across the basin toward the eastern boundary (Arhan et al., 2003; Garzoli et al., 2015; Palma & Matano, 2017; Stramma & England, 1999; van Sebille et al., 2012). The component on the western boundary returns to a more continuous flow by 34.5°S, although the DWBC at this latitude still exhibits large variability associated with the presence of westward propagating strong coherent vortices and/or Rossby wave-like signals (Garzoli et al.,

2015; Meinen et al., 2017; Valla et al., 2018). The interior NADW pathway originating near the Vitória-Trindade Ridge follows an eastward route that crosses the Mid-Atlantic Ridge between 20° and 25°S (Arhan et al., 2003; Garzoli et al., 2015; Speer et al., 1995; van Sebille et al., 2012) before proceeding to the Cape Basin and flowing southward along the African continental slope as a "Deep Eastern Boundary Current" (DEBC) of sorts (Arhan et al., 2003; Palma & Matano, 2017; Stramma & England, 1999). The climatological oxygen concentrations at 3,000 m (Figure 1b) from World Ocean Atlas (WOA; Garcia et al., 2014) outline the different paths of NADW with tongues of elevated oxygen concentrations along the western boundary and extending across the center of the basin.

With both the cold and the warm water routes of the upper MOC branches and a portion of the lower MOC branch passing through the Cape Basin, it is evident that this is a critical region for observing MOC-related flows. Recognition of the key roles that ocean dynamics in the Cape Basin play in the MOC is not new—Numerous previous experiments have studied aspects of the flows in the region using ship sections (e.g., Arhan et al., 2003; Duncombe Rae, 2005; Ganachaud, 2003; Gladyshev et al., 2008; Whittle et al., 2008), deep profiling floats (Lutjeharms et al., 1997; Richardson et al., 2003; van Aken et al., 2003), Argo float-altimetry syntheses (Majumder & Schmid, 2018; Rusciano et al., 2012; Schmid, 2014), and numerical models (e.g., Biastoch et al., 2009, 2015, 2018; Rimaud et al., 2012; Weijer & van Sebille, 2014). Historical in situ measurements using moored instruments in the region have been focused in the Agulhas Current and Agulhas Retroflection region farther east (Baker-Yeboah et al., 2009, 2010; Beal, 2009; Beal et al., 2015; Bryden et al., 2005) and in the greater Agulhas Current system farther south or north (Duncombe Rae et al., 1996; Garzoli & Gordon, 1996; Goni et al., 1997). The eastern components of SAMBA (SAMBA-East; Figures 1a and 1c, solid black line) represent the first direct in situ continuous full-water-column observations along 34.5°S covering the Cape Basin between the shelf break and the Walvis Ridge, near 0° longitude.

In the Cape Basin, the SAMBA-East moored instruments have provided continuous daily time series observations of the EBC system, their vertical structure, and their variability since 2013. Initially comprised of two bottom mounted acoustic Doppler current profiler (ADCP) moorings and eight Current and Pressure recording Inverted Echo Sounder (CPIES) moorings, SAMBA-East was further augmented in 2014 by the addition of four tall moorings equipped with temperature, salinity, and pressure sensors, as well as ADCP instruments (Ansorge et al., 2014; Kersalé et al., 2018). These observations provide the first opportunity to observe in detail the key EBC flows and their temporal and spatial variability as they carry components of the MOC across 34.5°S. In this study, we focus on the first ~23 months of data from September 2013 to July 2015 deployment of the SAMBA-East CPIES (Figure 1). The mean structure of the flow and associated volume transports from SAMBA-East will be compared to other available in situ data as well as to the output from an ocean general circulation model. This paper documents the EBC flow variability on timescales ranging from a few days to a few months. We also analyze the water mass properties carried by these currents and discuss possible causes for the largest observed upper and deep EBC variations.

2. Data and Methods

In order to assess the temporal variability of the EBCs in the South Atlantic, we analyze approximately 23 months of data from the array of CPIES deployed by the French "Institut Français de Recherche pour l'Exploitation de la Mer" and the South African Department of Environmental Affairs, Oceans and Coasts Division. The eight CPIES (see Table 1 and Figure 1c for locations) spread along 34.5°S from the continental shelf at the eastern edge of the Cape Basin (P1) out to the prime meridian (P8), spanning approximately 20° longitude with depths ranging from 1,300 m down to 5,200 m (Figures 1c). With the exceptions of the moorings at the shelf break, the typical spacing between the moorings is 3.75° in longitude. Note that CPIES P3 was lost during the 2015 July recovery cruise, so this study focuses on data from seven of the eight CPIES (Table 1).

A CPIES measures the current velocity 50 m above the bottom, the bottom pressure, and the round-trip time (τ) it takes an acoustic signal (12-kHz frequency) to travel vertically from the bottom-moored instrument to the sea surface and back. The use of the inverted echo sounder to observe the thermal variability of strong boundary currents has been ongoing for four to five decades (e.g., Garzoli, 1993; Rossby, 1969; Watts &

Table 1
CPIES Deployment Details

	CPIES 1 P1	CPIES 2 P2	CPIES 3 P3	CPIES 4 P4	CPIES 5 P5	CPIES 6 P6	CPIES 7 P7	CPIES 8 P8
Lat	34°24.35′S	34°29.81′S	34°29.96′S	34°30.25′S	34°30.00′S	34°30.42′S	34°29.92′S	34°30.06′S
Lon	17°33.46′E	17°18.04′E	17°8.31′E	15°0.16′E	11°12.19′E	7°27.03′E	3°43.15′E	0°0.02′E
Water Depth	1,266 m	2,129 m	2,850 m	4,482 m	4,969 m	5,185 m	5,030 m	4,608 m
Time Start 2013	Sep 7	Sep 7	No data	Sep 7	Sep 7	Sep 8	Sep 9	Sep 10
Time End 2015	Aug 11	Jul 22	No data	Aug 11	Aug 10	Aug 9	Aug 5	Aug 7

Note. CPIES = Current and Pressure recording Inverted Echo Sounders.

Johns, 1982; Watts & Rossby, 1977), and the addition in the 1990s of a pressure sensor to create the pressure-equipped inverted echo sounder (PIES) allowed for concurrent observations of the barotropic flows (e.g., Baker-Yeboah et al., 2009, 2010; Watts & Kontoyiannis, 1990; Watts et al., 1995). The development of the gravest empirical mode (GEM) technique for analyzing τ allowed arrays of PIES to be used to estimate the full-water-column profiles of temperature (T), salinity (S), and density and to quantify the baroclinic and barotropic geostrophic flows associated with surface intensified and subsurface intensified currents (Meinen & Watts, 2000; Meinen et al., 2004, 2009). As the methods for using PIES and CPIES to estimate absolute geostrophic velocities and full-water-column profiles of T, S, and specific volume anomaly (δ) have been widely discussed within the aforementioned literature, only a brief description of the technology and analysis will be provided here. Instead, the focus here is on how the methodology has been specifically applied to the Cape Basin region.

The GEM method is based on the use of hydrographic data collected in the region (from conductivity-temperature-depth [CTD] casts and Argo profiling floats) to create two-dimensional lookup tables of T, S, and δ as functions of pressure and travel time (e.g., Meinen & Watts, 2000; Watts et al., 2001). To create the lookup tables from the available hydrographic observations, a standard pressure level (1,000 dbar) was selected for the travel time integration. The first application of the GEM method to the CPIES in the SAMBA-East area was made by Meinen et al. (2013). The GEM lookup tables developed by Meinen et al. (2013) were based on a data set of 770 CTD and Argo profiles collected between 2009 and 2013, in the region bounded zonally by the continental shelf and 12°E and meridionally by 31°S and 37°S. For the present study, new GEM fields were created using CTD and Argo profiles up to the present day and spanning a larger zonal domain, from the continental shelf to 2°W (Figure 2a). The new GEM fields utilized all available Argo data (obtained from www.coriolis.eu.org) and all CTD profiles in the World Ocean Database (Boyer et al., 2013) collected within the above longitude-latitude boundaries. After excluding 15 profiles from these data sets that had clearly spurious salinities and temperatures, the total number of hydrographic profiles available was 5,593 (Figure 2b, black dots).

Inclusion of roughly seven times more profiles in building the GEM fields yields fairly similar lookup tables and accuracy estimates, and the estimates of T, S, and δ from the updated GEM fields and the original GEM fields are not statistically different (see Appendix A for an example of GEM field and more details). However, this larger data set allows for better coverage of the τ parameter space and more robust error statistics and furthermore demonstrates that the GEM fields are temporally stable (at least over the past ~35 years). Comparison of the T-S diagram from the updated GEM field (Figure 2b, colored dots) and the T-S diagram of the original hydrographic measurements (black dots) confirms that the GEM process has not created false water masses and contains all the structural features that are persistently and recurrently found in the region.

All hourly CPIES travel time, bottom pressure, and 50-m velocity measurements were low-pass filtered using a second-order Butterworth filter passed both forward and backward to avoid phase shifting—The cutoff period for the filter was 72 hr. Tidal response analysis (e.g., Donohue et al., 2010; Munk & Cartwright, 1966) determined semidiurnal and diurnal tidal bottom pressure constituents for each instrument; these tidal constituents were subtracted from the bottom pressure time series prior to filtering. The filtered travel time, bottom pressure, and velocity measurements were then subsampled to one value per day at midnight UTC. In addition to the CPIES data sets, concurrent CTD casts were collected along the transect during three

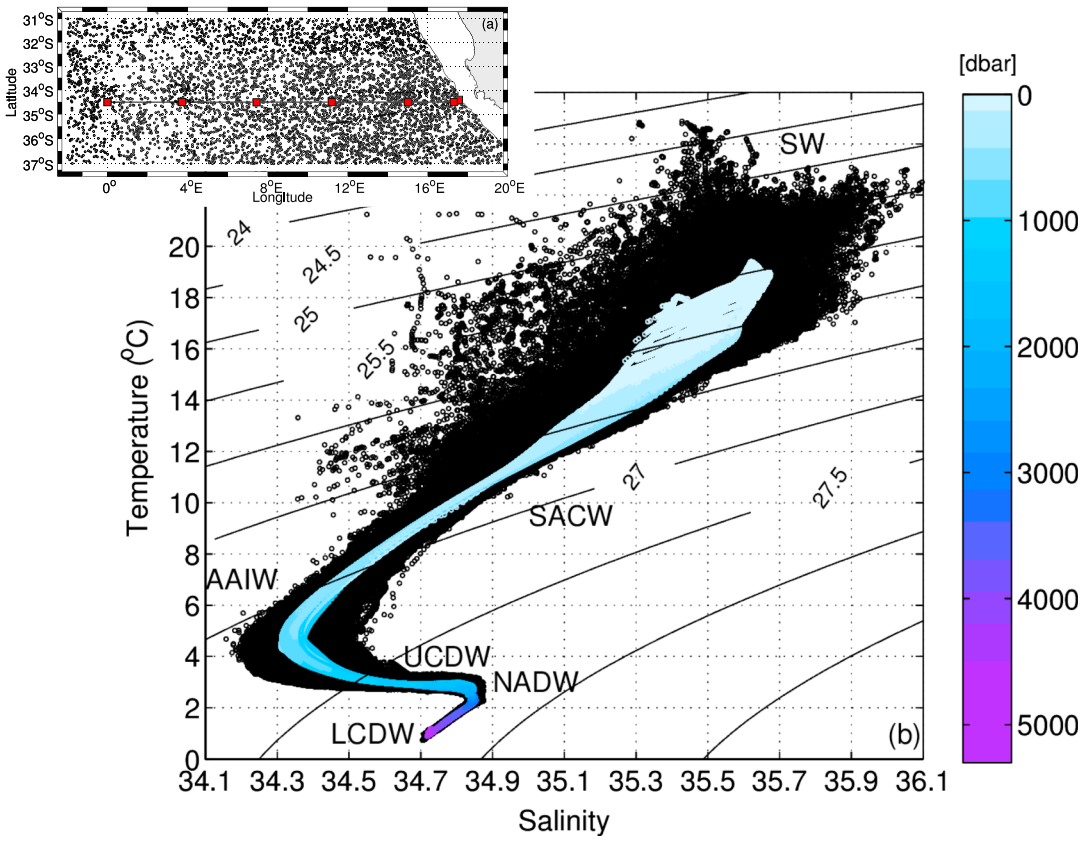

Figure 2. (a) Horizontal positions of the CPIES identified by the red squares along the SAMBA-East transect with black circles showing the positions of the CTD/Argo casts from 1983 to 2018 collected around the SAMBA-East transect and used to create the GEM field. (b) Comparison of the temperature (°C)-salinity relationship of CTD/Argo profiles (black circles) to the PIES-GEM estimated fields (pressure-colored circles). Key water masses (see section 3.1) are labeled. SW = surface water; SACW = South Atlantic Central Water; AAIW = Antarctic Intermediate Water; UCDW = Upper Circumpolar Deep Water; NADW = North Atlantic Deep Water; LCDW = Lower Circumpolar Deep Water; SAMBA = South Atlantic MOC Basin-wide Array; CPIES = Current and Pressure recording Inverted Echo Sounders; CTD = conductivity-temperature-depth; GEM = gravest empirical mode.

cruises on board the South African Research Vessel SA Agulhas II (September 2013, September 2014, and July 2015). CTD casts were conducted from the surface to within 5–10 m of the seafloor on each of the three cruises, with typically five casts offshore (between 0°E and 15°E) and five casts over the continental slope (between 15°E and 17°35′E). Full-depth CTD casts at each CPIES mooring location were used to calibrate each of the seven daily travel time records into the equivalent travel times at 1,000 dbar, the standard pressure level defined for the GEM lookup tables (e.g., Meinen & Watts, 1998). Then, the calibrated travel times at 1,000 dbar were combined with the GEM lookup tables to produce daily full-water-column profile estimates of T, S, and specific volume anomaly (δ) at each CPIES site. Note that the lookup tables are used to extrapolate the hydrographic profiles to the depth of the midpoint between each pair of CPIES to address bottom-triangle issues. Daily dynamic height anomaly profiles (Φ), relative to an arbitrary level of no motion, were then calculated at each site by vertically integrating δ profiles. Zonal gradients in Φ between neighboring CPIES yield full-water-column profiles of geostrophic velocity relative to an assumed level of no motion via the standard geostrophic method (e.g., Pond & Pickard, 1983); only the component of velocity that is orthogonal to the SAMBA-East transect is provided (e.g., Meinen et al., 2004, 2017).

To reference these flows to a level of known motion, the absolute geostrophic velocity at a reference level (hereafter referred to as the time-varying reference geostrophic velocity) is estimated from the zonal

gradients in bottom pressure between each CPIES (Meinen & Watts, 2000). However, the bottom pressure gradients only provide information about the temporal variability of the reference (also known as barotropic) flow and cannot be used to estimate the time mean due to the well-known leveling problem (e.g., Donohue et al., 2010). A time-mean reference velocity has to be added to the time-varying reference geostrophic velocity determined from the bottom pressure gradients. Unfortunately, the bottom current meters on the CPIES moorings are too far apart (>3.5° spacing) relative to the spatial decorrelation scales of the deep circulation (~1°; Donohue et al., 2010; Purkey & Johnson, 2010; Meinen et al., 2017) to use those to provide the time-mean velocity for the reference flows. As in previous studies in the South Atlantic (Meinen et al., 2013, 2017, 2018), the time-mean reference geostrophic velocity between pairs of CPIES was derived at 1,500 dbar from the output of a long (36-year) run of the Ocean general circulation model For the Earth Simulator (OFES; Masumoto et al., 2004; Sasaki et al., 2004, 2008) at eddy-resolving resolution. Combining the CPIES-GEM derived relative velocity profile time series with the time series of the reference velocity created by merging the model time-mean and bottom pressure-derived time-varying reference velocity yields estimates of the full-water-column time series of absolute geostrophic velocity between each pair of CPIES.

The following observational data sets are used herein for comparison with the time mean and variability of the EBCs derived from the CPIES travel time and bottom pressure observations (as described above):

- Direct measurements of velocity from the single-depth current meter of each CPIES (50 m above the seafloor);
- The 0.25° × 0.25° gridded mean dynamic topography over the 1993–2012 period produced by CLS-CNES (Rio et al., 2014);
- The Mesoscale Eddy Trajectory Atlas products produced by SSALTO/DUACS (www.aviso.altimetry.fr/)
- The 0.5° × 0.5° gridded absolute geostrophic velocity fields derived from a synthesis of all available Argo profiling float data together with satellite altimetry in the South Atlantic (Majumder et al., 2016; Majumder & Schmid, 2018; Schmid, 2014);
- Absolute geostrophic velocity fields obtained from transbasin XBT transects collected roughly along 34.5°S and extended to the ocean bottom using the WOA 2005 climatology with 0.25° horizontal resolution (e.g., Dong et al., 2009; Garzoli et al., 2013).

The model comparisons presented in this study are made with fields obtained from OFES. After a spin-up of 50 years, the model was forced with daily mean National Centers for Environmental Prediction/National Center for Atmospheric Research reanalysis atmospheric fluxes (Masumoto et al., 2004; Sasaki et al., 2004, 2008). The OFES outputs were provided by the Japan Agency for Marine-Earth Science and Technology through the Asia-Pacific Data Research Center at the University of Hawai'i at Mānoa. OFES output is available as 3-day snapshots from 1980 to 2015 at 0.1° horizontal resolution and on 54 vertical z levels. Note that this model has been extensively validated for the South Atlantic and used to study elements of the MOC in this region (Dong et al., 2011; Garzoli et al., 2015; Meinen et al., 2013, 2017; Perez et al., 2011; van Sebille et al., 2012). OFES means and standard deviations reported in this study are for the full 36-year record.

The energy spectral distributions of the EBCs, presented in section 3.3, are determined using the Welch's averaged periodogram method (Thomson & Emery, 2014). This method subsamples the time series into overlapping segments, here utilizing a 1-year window length with 6-month window overlap. A modified periodogram for each segment is computed, and the resulting periodograms are averaged to produce the estimate of the power spectral density.

3. Results and Discussion

3.1. Water Mass Properties and Mean Velocity

In order to address the origins of the waters carried by the EBCs, the hydrographic data are used to classify the different water masses in the region. Nominal water mass layers are shown on the average vertical sections of temperature (T), salinity (S), neutral density (γ^n), and dissolved oxygen (Figure 3). The different water masses discussed herein were classified according to the following commonly used definitions:

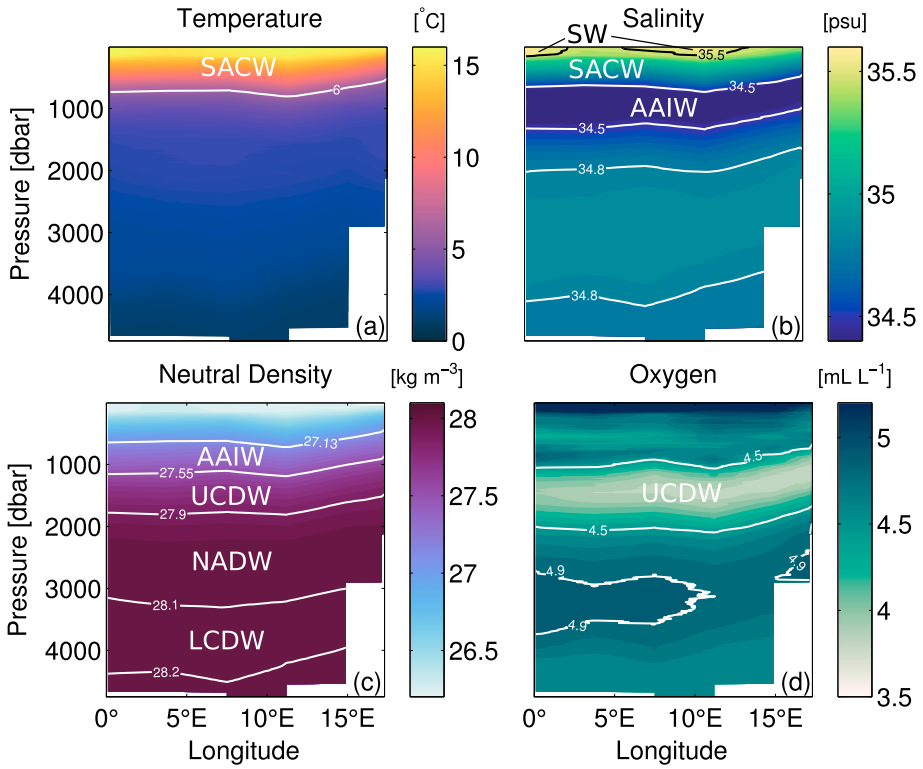

Figure 3. Average sections of in situ (a) temperature, (b) salinity, (c) neutral density, and (d) dissolved oxygen concentration from three cruises (September 2013, 2014, and August 2015) along the SAMBA-East transect. The approximate vertical distribution of key water masses (see section 3.1) are illustrated on their associated criteria parameters used for their classification. SACW = South Atlantic Central Water; AAIW = Antarctic Intermediate Water; UCDW = Upper Circumpolar Deep Water; NADW = North Atlantic Deep Water; LCDW = Lower Circumpolar Deep Water; SAMBA = South Atlantic MOC Basin-wide Array; SW = surface water.

- Surface water (SW): high-salinity ($S > 35.5$), high-temperature ($T > 16$ °C) water found at the surface in the South-East Atlantic as defined by Valentine et al. (1993);
- South Atlantic Central Water (SACW): This water enters the area as a blend of thermocline water and Subantarctic Surface Water from the south (Gordon, 1986; Valentine et al., 1993) with T between 6 and 16 °C and S between 34.5 and 35.5;
- AAIW: water mass with γ^n between 27.13 and 27.55 kg/m^3 and different S criteria defined by Rusciano et al. (2012) depending on their ocean of origin (Indian I-AAIW, $S \geq 34.3$; Indo-Atlantic IA-AAIW, $34.2 < S < 34.3$; Atlantic A-AAIW, $S \leq 34.2$). This distinction is useful to investigate the origin of the AAIW as different varieties originating from the South Atlantic and the Indian Ocean converge and mix in the southeast Atlantic;
- Upper Circumpolar Deep Water (UCDW): water mass with γ^n between 27.55 and 27.92 kg/m^3 (Heywood & King, 2002) and dissolved oxygen values below 4.5 ml/L. This water mass arises from the mixing of upwelled NADW with water circulating in the Antarctic Circumpolar Current. This water has a source region different from the overlying AAIW, but both water masses follow the same path, the cold water route;
- NADW: waters with γ^n between 27.92 and 28.11 kg/m^3 (Heywood & King, 2002);
- Lower Circumpolar Deep Water (LCDW): high-salinity lower circumpolar deep water (γ^n between 28.11 and 28.26 kg/m^3) that circulates around Antarctica with the ACC (Gladyshev et al., 2008; Heywood & King, 2002).

Evaluating the average vertical sections of T and S (Figures 3a and 3b), SACW dominates most of the upper water column between the surface and 700 dbar along much of the SAMBA-East transect. The only exceptions are two small areas where, using only the salinity criteria, two branches of SW centered at 1° and 11°E are found between the surface and 150 dbar (Figure 3b). Beneath the SACW, the density section is consistent

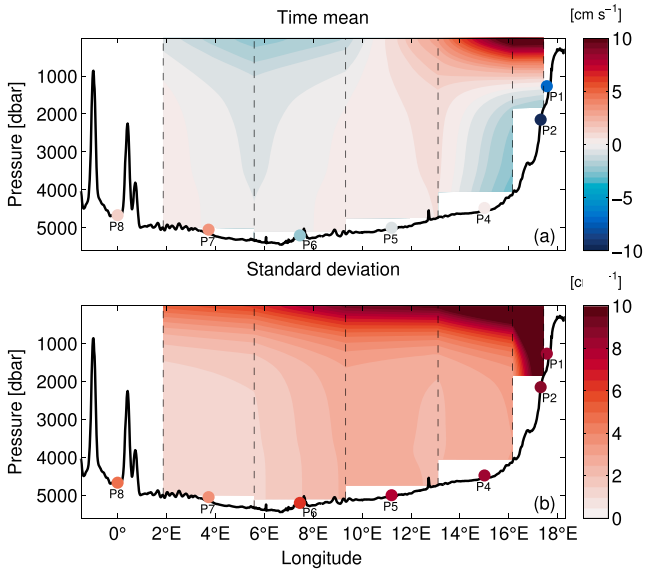

Figure 4. (a) Time-mean and (b) standard deviation of the absolute meridional geostrophic velocity (cm/s) determined between pairs of Current and Pressure recording Inverted Echo Sounders (CPIES). The colored dots represent the mean and the standard deviation of the direct measurement of velocity from the bottom current meters at the CPIES positions, respectively. Black vertical dotted lines denote the positions of the estimated geostrophic velocity profiles at the midpoints between CPIES.

with a layering of the water column by the intermediate and the three deep water masses defined above (Figure 3c). The low-salinity signature of AAIW (Figure 3b) and the low oxygen signature of UCDW (Figure 3d) are clearly visible in the mean sections. Salinities higher than 34.8 can be identified within the NADW layer along the entire transect (Figure 3b). Higher oxygen concentration of about 4.9 ml/L are found within the NADW layer between 0° and 11°E, and near the continental slope, indicating the presence of more recently ventilated waters (Figure 3d).

These different water masses converge in the eastern South Atlantic. The upper ocean circulation in this region is dominated by the Benguela Current, a broad, northward flowing current along the southwestern coast of Africa that forms the eastern limb of the South Atlantic Subtropical Gyre feeding the South Equatorial Current (e.g., Garzoli & Matano, 2011; Stramma & England, 1999). Previous observations along 34.5°S are limited, but historical measurements along 30°S revealed two regimes associated with the Benguela Current (Garzoli & Gordon, 1996): a nearly steady flow between the coast and 8°E and an offshore region filled with transient, alternating northward and southward flows between 8°E and the Walvis Ridge (0°), wherein the flow is essentially comprised of the integrated effects of transiting anticyclonic Agulhas Rings (e.g., Garzoli et al., 1997; Goni et al., 1997). Other observations in the region have indicated that no abrupt change due to Agulhas Rings is observed across the steady flow, but the horizontal gradient between warm water from the Agulhas leakage and cold water from the coastal upwelling regime can generate a shelf edge current (e.g., Bang & Andrews, 1974; Veitch & Penven, 2017). This strong equatorward jet, called Cape Peninsula Jet or Good Hope Jet, is located over the shelf-break (mean position: 34°S, 18°E), with a width of 20–30 km, and has been shown to reach speeds of 50 cm/s (e. g., Peterson & Stramma, 1991; Shannon & Nelson, 1996; Shillington et al., 2006). The SAMBA-East array, however, is located at the western edge of the jet and so is too far offshore to consistently capture/observe the whole jet structure.

The time-mean absolute geostrophic velocity section obtained from the CPIES data at 34.5°S shows a positive (northward) flow between P5 and P1 (11–17.5°E), covering an area 580 km wide and about 1,270 dbar deep over the continental slope (Figure 4a). This flow corresponds well to the steady part of the Benguela Current found in earlier studies. The estimated near surface mean velocities associated with this current decrease from 10.7 cm/s on the upper part of the slope (between P1 and P2, 17.5–17.3°E) to 3.2 cm/s offshore (between P4 and P5, 15–11°E). The higher mean velocity in-shore may be influenced by the Cape Peninsula Jet, although P1 is located offshore of the mean position of the jet. Further west, between 2°E and 9°E, the mean surface flow is weak and southward with velocity around 2 cm/s. This flow, in the opposite direction of the Benguela Current, is consistent with the transient flow previously observed offshore of the steady component of the Benguela Current (Garzoli & Gordon, 1996). Remember that the velocities here are geostrophic estimates that represent the average flow between pairs of CPIES nearly 4° of longitude apart, and they do not include the wind-driven Ekman velocity. Direct measurements with lowered or hull-mounted ADCP or other direct measurement devices which measure total velocity at finer spatial resolution would be expected to capture mean flows with larger amplitudes near the surface and more spatial variability.

Below the upper layer, the DEBC has been observed by a few previous studies in the region, sometimes referred to as a poleward undercurrent or the Benguela Undercurrent (Lass & Mohrholz, 2008; Nelson, 1989). This southward current has been observed as far south as 35°S along the western coast of Africa from sparse observations (Baker-Yeboah et al., 2010; Majumder & Schmid, 2018; Nelson, 1989; Schmid, 2014) and has also been noted in modeling studies (Garzoli & Matano, 2011; Palma & Matano, 2017; Stramma & England, 1999; Veitch et al., 2010). There is less of a consensus about whether or not this current exits the South Atlantic, travels around the southern tip of Africa, and enters the Indian Ocean (Arhan et al., 2003; Speer et al., 1995).

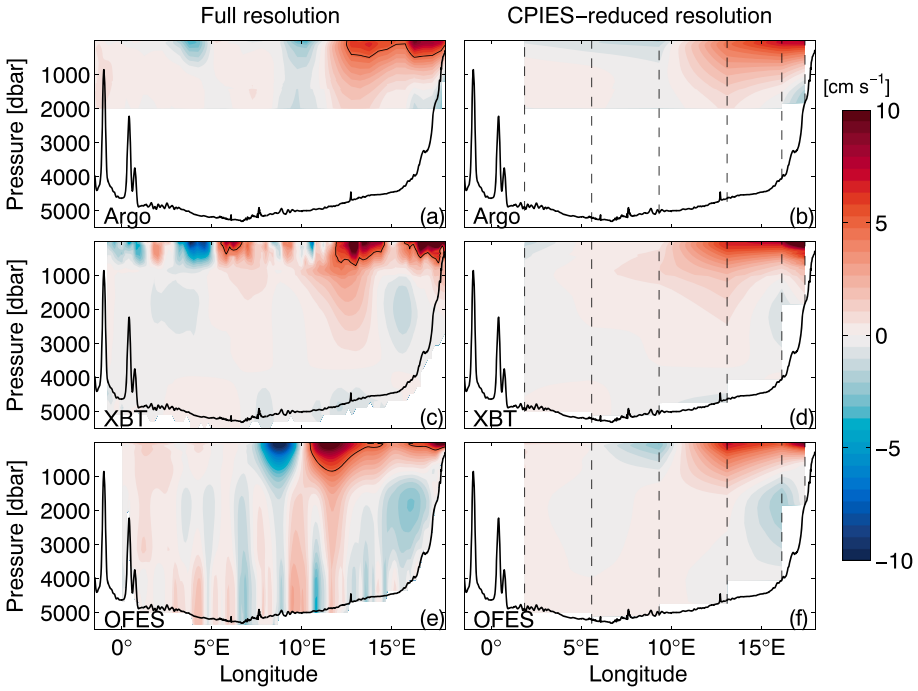

Figure 5. Time-mean of the absolute meridional velocity (cm/s) from Argo/altimetry synthesis (a, b), XBT/WOA (c, d), and OFES model output (e, f). The left column shows the data with their full spatial resolutions; while the right column shows the same data with the CPIES-reduced spatial resolution for a better comparison. The black lines on the sections (a, c, e) represent the 5 cm/s contour of the time-mean absolute meridional velocity. XBT = expendable bathythermograph; WOA = World Ocean Atlas; OFES = Ocean general circulation model For the Earth Simulator

In the new time-mean results presented herein, the DEBC is observed as a southward flow below 1,270 dbar extending from the continental slope offshore between P1 and P4 (17.5–15°E), with a peak mean absolute geostrophic southward velocity of 3.0 cm/s (Figure 4a). The velocity from the near-bottom current meters (Figure 4a, colored circles) can be qualitatively compared to the geostrophic velocities. Keep in mind that the velocity from the current meter is a point measurement and the geostrophic velocity represents horizontal averages between each pair of CPIES. The time-mean coincident direct current meter estimates show near-bottom velocities of 0 cm/s at P4 (15°E) and southward velocities in the upper part of the slope, 17.5–17.3°E (−10.3 cm/s at P2 and −7.2 cm/s at P1). As expected, the direct near-bottom point velocities are stronger than the CPIES geostrophic velocities (an integrated measurement), but the basic flow patterns and flow directions are similar. This supports the presence of a mean southward DEBC over the continental slope at 34.5°S and provides confidence in the CPIES geostrophic velocities.

To further validate the mean velocity structure from the CPIES-GEM results, the mean meridional velocity sections from two ancillary data sets and from the OFES model were examined. Since the OFES model is used to provide the time-mean velocity for the reference CPIES-GEM flow, this comparison is not completely independent. Recall, however, that the time-mean OFES results are only used at one depth, so the vertical structure information in the time-mean OFES section is fully independent. The zonal and vertical structures of the mean meridional velocity sections from the Argo/altimetry synthesis (Figure 5a), the XBT/WOA (Figure 5c), and OFES (Figure 5e) generally compare well with the mean section from the CPIES-GEM data (Figure 4a). As expected, these three mean sections capture finer horizontal scales than are present in the CPIES-GEM mean section due to their finer horizontal resolution. In particular, these products capture two potentially independent cores in the steady part of the Benguela Current, one between 10°E and 15°E and one between 15°E and the African coast. These two distinct Benguela Current cores are not resolved by the CPIES array, because of the large distance between pairs of CPIES. To look at similar scales, the velocities from the Argo/altimetry synthesis, XBT/WOA analysis, and OFES model output are averaged between the longitudes of the pairs of CPIES to simulate the geostrophic averaging inherent in the CPIES-GEM technique. These smoother sections (Figures 5b, 5d, and 5f) are very

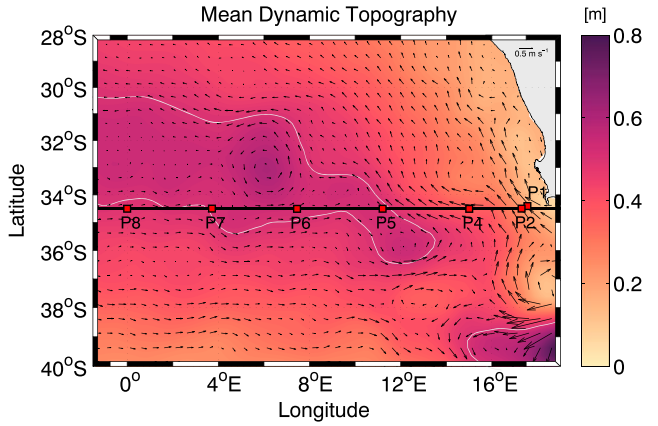

Figure 6. Mean dynamic topography (m) and geostrophic velocity field from 1993 to 2012. The black line denotes the position of the South Atlantic MOC Basin-Wide Array-East transect and the red squares represent the Current and Pressure recording Inverted Echo Sounders positions. White lines highlight the 0.5-m isolines of mean dynamic topography.

similar to the CPIES-GEM mean section (Figure 4a) in terms of horizontal and vertical extents of the Benguela Current, particularly above 1,500 dbar and inshore of 11°E. The two cores of the Benguela Current are still present in the XBT/WOA product and OFES model, but not in the Argo/altimetry synthesis. The weak offshore poleward surface flow, in the opposite direction of the Benguela Current, that is observed in the CPIES-GEM mean velocities (Figure 4a) is also observed in the Argo/altimetry synthesis (Figure 5a) and the OFES model (Figure 5e) between 8° and 11°E, and further offshore (between 3° and 5°E) in the XBT section (Figure 5c), but is substantially weakened in the smoothed sections (Figures 5b, 5d, and 5f). The Argo/altimetry synthesis provides no data below 2,000 dbar, and the XBT/WOA product is based solely on climatology below roughly 800 dbar. Nevertheless, both observational products and OFES model provide hints of the DEBC inshore of 12°E (Figures 5a, 5c, and 5e) as observed by the CPIES-GEM observations (Figure 4a). It must be noted that the temporal averaging windows of each of these products differ from one another and from the CPIES records (~2 years of daily data for CPIES, 36 years of 3-day snapshots for OFES, 23 years of monthly means for Argo/altimetry synthesis, and 23 snapshots over 16 years for XBT/WOA), so perfect agreement between the mean sections is not to be expected.

Satellite and hydrography derived mean dynamic topography from AVISO and the associated geostrophic velocity field (Figure 6) provide added spatial context for the upper ocean flow observed along 34.5°S (Figures 4a and 5). The surface geostrophic flow from AVISO reveals the steady part of the Benguela current, characterized by two cores along 34.5°S, which are actually two branches separated by a cyclonic circulation located farther north (center at 33.5°S, 15°E). These fields also illustrate why the offshore branch might not appear as clearly in the CPIES-GEM data. Indeed, the mean dynamic topography map indicates that the inshore Benguela branch has a north-northwestward direction and passes between P4 and P1, consistent with what is observed by the CPIES, whereas the offshore Benguela branch between P5 and P4 is characterized by a closer-to-zonal orientation. This flow will understandably not be well represented in the CPIES-GEM data, which can only capture the component of the geostrophic flow that is orthogonal to the CPIES array (i.e., the meridional component). On the western edge of the Agulhas eddy corridor, offshore of P5, the mean geostrophic velocity map derived from the AVISO data (Figure 6) illustrates how passing anticyclonic eddies affect the mean flow field creating east-southeastward flow in this region, which explains the CPIES observed weak mean southward flow measured between P8 and P5.

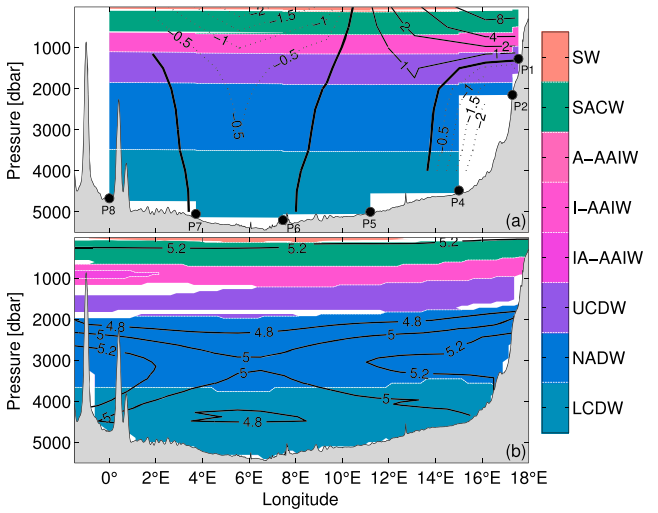

Figure 7. (a) Schematic section illustrating the observed water masses. Water masses are determined using the PIES-GEM estimated profiles. Contours of the time-mean absolute meridional geostrophic velocity determined between pairs of CPIES are represented (solid bold line: Zero-contour, solid line: Northward flow, dotted line: Southward flow). (b) Same as (a) from the WOA climatology and including dissolved oxygen criteria to identify water masses. The black contours show the oxygen concentration [mL L^{-1}]. The white areas represent water masses with characteristics different than the ones defined in Section 3.1. SACW = South Atlantic Central Water; AAIW = Antarctic Intermediate Water; UCDW = Upper Circumpolar Deep Water; NADW = North Atlantic Deep Water; LCDW = Lower Circumpolar Deep Water; SW = surface water; CPIES = Current and Pressure recording Inverted Echo Sounders; PIES = pressure-equipped inverted echo sounder; GEM = gravest empirical mode.

To illustrate which water masses the Benguela Current and the DEBC carry in a time-mean sense, we superimposed the time-average locations of the main water mass interfaces, inferred from the CPIES-GEM *T*, *S*, and density profiles, on the time-mean meridional velocity section (Figure 7a). Note the CPIES-GEM time-mean properties represent an average over a 2-year period, and they do not include dissolved oxygen, which is crucial for identifying recently ventilated NADW. To evaluate the robustness of the mean water mass interface locations from the CPIES-GEM data, and to include information about dissolved oxygen, we also calculated the time-mean locations of the main water mass interfaces from the WOA climatology (Figure 7b). Overall, the time-mean locations of the main water masses do not fit with a preferential northward or

southward flow. This banded flow pattern has been observed at the western boundary at 34.5°S and revealed the presence of recirculation, and/or strong mixing in the area (Meinen et al., 2017; Valla et al., 2018).

In the upper layer, the mean CPIES-GEM and WOA sections reveal the presence of SW from the surface to about 100 dbar using its salinity and temperature criteria, and SACW from 100 to 650 dbar (also fairly consistent with the average from the three CTD sections presented in Figure 3). These two water masses are transported southward across the transect between the Walvis Ridge (P8) and 11°E (P5), and northward between 11°E and the continental shelf (P1). The time-mean northward direction of the SW and SACW flows east of 11°E is consistent with one of the upper limb MOC pathways (warm water route; see section 1) passing through the Cape Basin.

The intermediate water column, from 650 to 1,100 dbar, is dominated by the presence of I-AAIW (Figure 7a). Just like the near surface water masses, the I-AAIW is carried southward between Walvis Ridge and 11°E and northward between 11°E and the continental shelf. The longer-term average water mass interface locations determined from the WOA climatology section are in general quite similar to those determined from the CPIES-GEM data (Figure 7b), although the WOA climatology does suggest that over a longer-term period one might expect to see IA-AAIW near the Walvis Ridge.

Concerning the deep waters, UCDW is detected in the mean section from 1,100 to 1,900 dbar (Figure 7a). Although the dissolved oxygen criteria for UCDW (concentrations below 4.5 ml/L) cannot be tested using the CPIES-GEM data, the depth range of this water mass determined purely from the neutral density criteria agrees well with the depth range inferred from the WOA climatology utilizing both the density and oxygen criteria (Figure 7b). NADW is found between 1,900 and 3,400 dbar, while LCDW fills the depths below 3,400 dbar. There is little vertical shear in the deep layers (Figure 7a), and the mean section shows the UCDW, NADW, and LCDW being carried alternately southward and northward in a banded pattern over most of the basin west of 14°E. This pattern possibly indicates a recirculation cell similar to that which has been observed further north in the Angola Basin by Arhan et al. (2003), or more recently by Majumder and Schmid (2018), centered at 33°S, 6°E. Alternatively, the banded flow pattern offshore may also simply reflect the rectification onto the mean flow caused by averaging of the Agulhas Rings that transit through the region, as their influence can be felt from the surface down to a maximal observed depth of 4,000 m (van Aken et al., 2003). The southward DEBC east of 14°E is noticeably stronger than the banded deep flows offshore (Figure 4a), and interestingly, the WOA oxygen concentration climatology across this section (Figure 7b) and the average of the CTD sections (Figure 3d) both indicate the presence of recently ventilated NADW water at the location of the DEBC adjacent to the continental slope. The presence of these higher dissolved oxygen values (concentrations above 5.2 ml/L, typical of recently ventilated NADW in the western South Atlantic—Figure 1b) suggests that these waters have been in contact with the surface more recently than is expected for deep water masses in this region. This result is therefore consistent with the hypothesis that the DEBC is connected to an interior pathway bringing recently ventilated NADW waters across to the eastern boundary, as there are no alternative sources of oxygen-enriched waters within these density layers (Arhan et al., 2003; Garzoli et al., 2015). Note elevated dissolved oxygen values at level of NADW and LCDW are also found between 10°E and Walvis Ridge in the average CTD sections (Figure 3d) and near Walvis Ridge in the WOA climatology (Figure 7b), suggesting some additional mixing/recirculation within the Cape Basin.

3.2. Temporal Variability

The strongest variability in the geostrophic velocities in the upper layer is found near the coastline (between P1 and P2), with a standard deviation from the daily time series of 36.4 cm/s (Figure 4b) that greatly exceeds the mean value of 10.7 cm/s (Figure 4a). This high variability is consistent with previous observations of the Cape Peninsula Jet, at least in our case the western boundary of the jet, which exhibits strong variability in its location and intensity (Boyd & Nelson, 1998; Veitch et al., 2017). The observed standard deviation pattern of high variability inshore and lower variability offshore is consistent with the location of the Benguela Current in historical studies (Garzoli & Gordon, 1996; Veitch et al., 2017).

The variability of the flow in the deep layer, below 2,000 dbar, is strongest between P2 (17.3°E) and P4 (15°E) in the DEBC, with a maximum standard deviation of 3.2 cm/s. It is nearly as large between P5 and P6 (11–7°E), with a maximum standard deviation of 2.9 cm/s. However, the variability in the deep layer is

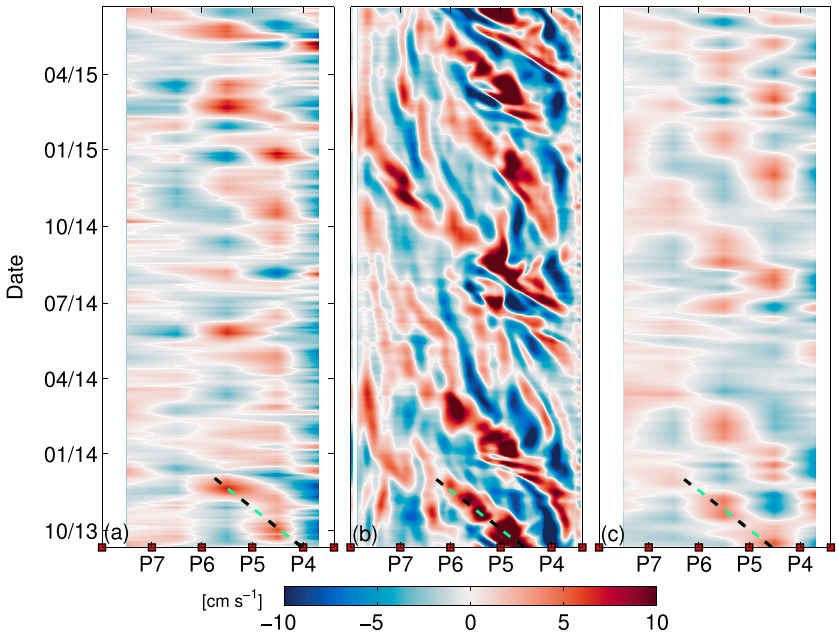

Figure 8. Hovmoller plots illustrating the absolute meridional geostrophic velocity at 2,700 dbar for the offshore portion of the domain (a) from the Current and Pressure recording Inverted Echo Sounders (CPIES), and (b, c) from the Ocean general circulation model For the Earth Simulator output (b, full resolution; c, CPIES-reduced spatial resolution). White contour indicates zero meridional flow. Red squares along the bottom axes indicate the location of the CPIES. Green and black dashed lines illustrate the westward component of the propagation speed of Agulhas Rings.

fairly uniform compared with the upper layer (Figure 4b). The concurrent direct current meter estimates show less variability from the standard deviation between P8 and P6 (from 3.5 to 6.3 cm/s) compared to the inshore part of the transect (from P5 to P1) where the standard deviation is about 8 cm/s. Recall that the direct current meters represent point measurements in the horizontal scale, while the geostrophic velocities between pairs of CPIES represent an average over nearly 4° of longitude. For both the point measurements and the geostrophic estimates, the velocity variability below 2,000 dbar is much larger than the mean flow for these 2 years, illustrating the important role of Agulhas Rings, eddies, and other transient features in this region.

Previous work at the western boundary at 34.5°S has shown that the dominant source of variability in those boundary currents is westward propagation of Rossby wave-like features toward the boundary from the basin interior (e.g., Meinen et al., 2017). Westward propagating signals in the eastern South Atlantic have been observed from altimeter and radiometer records between 10.5°S and 24.5°S (Oliveira & Polito, 2013). According to that study, the dominant variability source switches south of 24.5°S from Rossby wave variability to variability associated with Agulhas Rings. A Hovmoller plot can be used to examine these propagating signals. The meridional velocity at 2,700 dbar (Figure 8a) shows significant 5–10 cm/s velocity fluctuations that persist for a month or longer and propagate westward. It needs to be noted that the actual propagation is northwestward along the Agulhas Ring corridor (Dencausse et al., 2010; Garzoli & Gordon, 1996), but only the westward component of propagation can be detected with a zonal array of moored instruments.

One way to better resolve the zonal structure of the propagating features would be to look at satellite altimetry fields; however, previous work has shown that subsurface rings might represent a portion of the features and that they are poorly resolved by altimetry (e.g., Goni & Johns, 2003). An alternative tool to evaluate deep propagating features is the OFES model. The OFES output, which has 0.1° horizontal resolution, was used to evaluate the sources of variations of the deep flow and the propagation of the features in the model simulation. Hovmoller plots of the OFES meridional velocity at 2,700 dbar across 34.5°S (Figure 8b) illustrate clearly the presence of alternating bands of flow associated with Agulhas Rings propagating westward from P4 to P7 (again only the westward component of northwestward propagation is examined here, as the

mooring array is zonal). These anticyclonic eddies are associated with northward velocities on their eastern side and southward velocities on their western side. It needs to be noted that mesoscale variations in a model that does not assimilate observations are not expected to be in phase with mesoscale variations in the real ocean but it is the frequency, periodicity, propagation, and structure of such events in the model that is of interest for comparison. Over the full time period record (September 2013 to July 2015), five events are detected clearly (Figure 8b) in the model output. These events are identified between P4 and P6 from September to December 2013, from January to March 2014, from July to September 2014, from November 2014 to January 2015, and from February to April 2015, with each event having a duration of approximately 3 months. The higher spatial resolution in the model is evident; propagating features do not show up as clearly in the observed data (Figure 8a) as in the fully resolved model (Figure 8b), due to the CPIES geostrophic averaging. If the OFES output is averaged between the longitudes of the CPIES to simulate the CPIES geostrophic velocities (Figure 8c), the resulting Hovmoller looks much more like the data (Figure 8a). Nevertheless, in the averaged OFES Hovmoller, five propagating events with positive velocities and similar propagation speeds as those observed in the full-resolution model output are still present (e.g., January 2014), although their amplitudes are reduced and their zonal structure is degraded.

An analysis of lagged correlations of the meridional velocity at 2,700 dbar was performed in order to estimate the westward component of the propagation speed of these eddies both in the model output and in the data (not shown). The resulting propagation speed was roughly −6.7 km/day in the model, and −7.2 km/day in the observations (negative indicating westward; illustrated by the dashed lines in Figure 8) in good agreement with one another. Both values fall within the range of previous estimates of −2.9 to −7.3 km/day for Agulhas Ring translation through this region (e.g., Byrne et al., 1995; Goni et al., 1997; Olson & Evans, 1986; Schouten et al., 2000). The propagation speed is faster than the westward propagating features on the western boundary in OFES that were reported for SAMBA-West in Meinen et al. (2017) as about −2.5 to −3.5 km/day and were linked to Rossby wave-like features. The wider spacing between CPIES in SAMBA-East and SAMBA-West makes it somewhat difficult to ascribe the sources of the observed variability in the deep layer; however, we can confirm that the observed propagation in the SAMBA-East region is dominated by the passage of Agulhas Rings.

Another interesting feature of the flow variability across the SAMBA-East line at 2,700 dbar is evident in the observations (Figure 8a). There is the tendency to observe strong southward flows east of P4 at the times when Agulhas Rings are being observed offshore of P4. A similar pattern is also present in the model output (Figures 8b and 8c), but the southward flows have weaker magnitudes when the model fields are smoothed to match the spacing/geostrophic averaging of the CPIES array (Figure 8c). The paired inshore flows-offshore Agulhas Rings in the observations and model results is in agreement with the results of an earlier study of van Sebille et al. (2012) using a shorter segment of the same OFES run used herein, which suggested that the southward DEBC in the Cape Basin could be somewhat intermittent and that variations in the DEBC flow might be directly linked to the passing of Agulhas Rings.

3.3. EBC Transport and Energy Spectral Distribution

Absolute meridional geostrophic velocity fields are used to construct estimates of the two EBC transports. Defining the zonal and vertical boundaries of the Benguela Current and the DEBC is unavoidably somewhat subjective. Stramma and Peterson (1989) defined the longitudinal border of the Benguela Current at 32°S as being close to 10°E. Offshore of this longitude, and in agreement with our observations, Stramma and Peterson (1989) pointed out that Agulhas Rings strongly influence the ocean flow. Difficulty in defining the boundaries of a coherent flow is a common problem in quantifying the transport of individual ocean currents (e.g., Hogg & Johns, 1995). It has been often documented with western boundary currents that strong propagating ocean signals (e.g., Rossby wave-like features and coastally trapped waves) can become inextricably intertwined with the boundary current when calculating transports (e.g., Meinen et al., 2017; Mooers et al., 2005). Eastern boundary current transports are similarly affected by alongshore propagating features (e.g., Fennel, 1999; Illig et al., 2018; Schumann & Brink, 1990). For this study, we calculate the EBC transports within the horizontal boundaries suggested by the mean meridional velocity section (Figure 4a); that is, Benguela Current transports will be calculated between P5 and P1 (11–17.5°E), and no distinction will be made between the northward flowing Benguela Current and potential contributions from the northward flowing Cape Peninsula Jet. The DEBC transports will be calculated between P4 and P1 (15–17.5°E). The

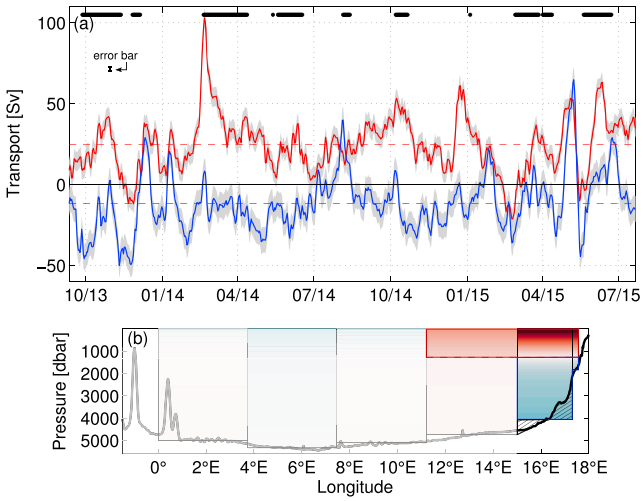

Figure 9. (a) Time series of absolute transport (Sv) calculated for the Benguela Current (upper part, red line) and the deep eastern boundary current (lower part, blue line) with estimated daily accuracy estimates (gray shading) as derived in Appendix B. Black vertical error bar at left illustrates the estimated bias accuracy as discussed in the Appendix B. The time-mean values of the upper and lower part are identified by the horizontal dashed lines. The black dots at the top indicate the presence of an Agulhas Rings less than 150 km from P5. (b) Areas used to calculate the transport (red box, Benguela Current transport; blue box, deep eastern boundary current transport). The graduated colors within each box represent the time-mean profile of the absolute meridional geostrophic velocity. The two hatched triangles are defined with identical areas to reduce the classical bottom-triangle issue.

DEBC integration domain is also consistent with the boundaries of the enhanced oxygen signals associated with recently ventilated NADW (Figures 3d and 7b).

To examine the flow variability of the Benguela Current, the volume transport is integrated between the surface and 1,270 dbar, while the DEBC transport is integrated between 1,270 dbar and the bottom. The character of the transport time series is not sensitive to modest changes in these integration limits. Different techniques can be applied to estimate the deep transport due to the classical "bottom-triangle" issue. This will be particularly important in this analysis due to the large bottom triangle between P2 and P4 (Figure 4a), where the steepest sloping topography is found. Deep transports between P1 and P4 have been calculated by two different ways, illustrated here via the example of the P2 to P4 span. First, the CPIES-GEM hydrography-derived lookup tables were used to extrapolate the dynamic height profile at P2 to the topographic depth where the area between P4 and the midpoint of the P4-P2 span equals the area between the midpoint of the P4-P2 span and P2 (as depicted in Figure 9b with hatched areas). The second method tested involves "filling" the bottom triangle in a similar manner by assuming a constant flow (i.e., zero vertical shear) below the deepest common depth of sites P2 and P4 and the bottom instead of using the GEM lookup tables. The actual variances of the deep transport time series between P2 and P4 that result from these two methods is 302 and 343 Sv^2 (1 Sv = 10^6 m^3/s), respectively, while the variance associated with the difference between the time series is just 12.9 Sv^2. The correlation between time series estimated via the two methods is $r = 0.98$, and the mean difference is 2.4 Sv. This demonstrates that while it is quite important to address the bottom-triangle issue, the resulting integrated transport mean and variability are not very sensitive to the method used for filling in the transports in the bottom triangle. For the analysis that follows, we use the first method.

The resulting Benguela Current (Figure 9a, red line) and DEBC (Figure 9a, blue line) volume transports demonstrate strong variations at a wide range of time scales. While it is clear that Agulhas Rings and other surface-trapped or surface-intensified features can simultaneously impact the shallower and deeper flows, a meaningfully robust relationship between the upper and lower EBC is not evident during this 2-year period. The correlation coefficient between the Benguela Current and DEBC transport time series is $r = 0.4$, which is significantly different from zero at the 95% confidence level based on the number of degrees of freedom (Thomson & Emery, 2014). The number of degrees of freedom is estimated by dividing the record length by twice the observed integral time scales (50 and 30 days for the Benguela Current and DEBC time series). Despite being statistically significant, the relationship between the two currents obviously does not explain a large percentage of the observed variance (~16%). Variations in the offshore location of the Agulhas Rings passing through the array, their changing intensity, and their interactions with other mesoscale eddies complicate the upper and lower EBC transport time series. Identifying a definite causal relationship between these two transport time series will likely require a longer time series and will be the subject of a future study.

The Benguela Current northward transport is characterized by a mean value of 24 Sv and a daily standard deviation of 17 Sv (Table 2). These values are in good agreement with the estimations from the OFES model output integrated within the same longitude and pressure limits for the

Table 2
Mean Value, Standard Deviation, and Peak-to-Peak Range of the Benguela Current and DEBC Absolute Transport (Sv) From CPIES, Argo/Altimetry Synthesis, XBT/WOA and OFES Output Integrated Within the Same Longitude-Pressure Bounds

	Mean (Sv)		STD (Sv)		Peak to peak range (Sv)	
	Benguela	DEBC	Benguela	DEBC	Benguela	DEBC
CPIES	25	−12	17	17	124	115
Argo/altimetry	25	n.a.	4	n.a.	21	n.a.
XBT/WOA	26	n.a.	6	n.a.	22	n.a.
OFES	22	−7	23	13	140	106

Note. CPIES = Current and Pressure recording Inverted Echo Sounders; DEBC = deep eastern boundary current; XBT = expendable bathythermograph; WOA = World Ocean Atlas; OFES = Ocean general circulation model For the Earth Simulator; STD = standard deviation; n.a. = not applicable.

full 36-year record (mean of 22 Sv and 3-day snapshot standard deviation of 23 Sv). Again, note that this comparison is not fully independent, as the model time-mean velocity is used to reference the CPIES-GEM flow at the bottom. A simple Monte Carlo-style test using 4,000 random 23-month subsets of the 36-year model record suggests that a record of 23 months length in the model could have a mean transport value between 12 and 29 Sv. This range of values is associated with a standard deviation of 3 Sv, which can explain the differences between the full 36-year record from the OFES model output and the CPIES observations. Similar integrated transport mean values (25 and 26 Sv), but much lower standard deviations (4 and 6 Sv), are estimated for the Benguela Current from the Argo/altimetry synthesis and XBT/WOA products, respectively, when integrated within the same longitude-pressure bounds. The smaller temporal standard deviations for Argo/altimetry synthesis and XBT/WOA products are to be expected, given the reduced temporal resolution of those products (Argo/altimetry synthesis: monthly; XBT/WOA: approximately four transects per year) versus the CPIES observations (daily) and OFES fields (3-day snapshots). The reduced resolution is not the only source of difference, however, as subsampling the CPIES observations to monthly values only reduces the standard deviation from 17 to 12 Sv.

The mean Benguela Current transport estimates presented herein (CPIES, Argo/altimetry synthesis, XBT/WOA, and OFES) all fall within the 15- to 25-Sv range of previously published estimates of the Benguela Current transport (Garzoli et al., 1997, 2013; Gordon et al., 1992; Majumder & Schmid, 2018; Sloyan & Rintoul, 2001; Stramma & Peterson, 1989). Note that if the much broader (zonally) integration limits used by Garzoli et al. (2013) are applied to the CPIES data presented here, the resulting time-mean Benguela Current transport estimate is still within the range of the historical estimates (15 Sv). The daily variability of the Benguela Current from the CPIES data exhibits a total peak-to-peak range of roughly 124 Sv, greatly exceeding all previous estimates of the Benguela Current transport variability. Indeed, the only transport time series with similar length scale using moored instruments surrounding the SAMBA-East transect shows a peak-to-peak range of only 40 Sv (Garzoli & Gordon, 1996). Similar to the Garzoli and Gordon (1996) study, the largest variations in Benguela Current transport in our data set appear to be mainly associated with the presence of intense mesoscale eddies. This has been confirmed through comparison to the mesoscale eddies in the region at these times using the Mesoscale Eddy Trajectory Atlas product based on an eddy-tracking methodology developed by Chelton et al. (2011). The maximum values of the Benguela Current transport are recorded during times when Agulhas Rings with a typical radius of 100 km are located close to P5, with a distance between the Ring center and the mooring location less than 150 km (Figure 9a, black dots).

The DEBC transport estimated from the CPIES is also very energetic, with a peak-to-peak range of nearly 115 Sv (Table 2), from a maximum southward transport of 50 Sv in November 2013 to a northward transport of about 65 Sv in May 2015 (Figure 9a). This last northward event has been studied in more detail in a parallel analysis of the data from the tall moorings deployed near the continental slope over the SAMBA-East transect (Kersalé et al., 2018). The results of that parallel analysis suggest that the presence of an intense dipole during this time period leads to strong north-northwestward currents over the whole water column.

Of particular interest for the present study are the periods when the southward transport of the DEBC intensifies. These southward pulses in the deep transport are often observed approximately 20 days after anomalous northward transport episodes in the upper layer, which are associated with the propagation of Agulhas Rings further offshore. The correlation between the transports was maximum at a 22-day lag ($r = 0.55$ and significant at 95% level). The origin of these pulses of deep flow has already been linked, in the OFES model, with the propagation of Agulhas Rings in the study of van Sebille et al. (2012), and this interpretation is further supported by the Hovmoller analysis of the meridional velocity at 2,700 dbar discussed earlier (Figure 8). Despite the presence of Agulhas Rings, and dipoles, the DEBC time-mean transport is southward (-12 ± 17 Sv; see Table 2). The time-mean value is roughly consistent with the sole documented historical estimate of transport for the DEBC at 35°S (-11 ± 4 Sv) by Arhan et al. (2003). The Argo/altimetry synthesis and the XBT/WOA products shown herein cannot provide a time-variant transport estimate for the DEBC (the former because it does not extend to large enough depths and the latter because it relies on climatology below about 800 m). The OFES model output yields a DEBC with a time mean, −7 Sv, that is approximately 42% smaller than the observed CPIES estimate, with a smaller standard deviation (13 Sv). As for the Benguela Current transport, a simple Monte Carlo-style test has been done for the DEBC. This test finds mean DEBC transport values ranging between −1 and −15 Sv, and a standard deviation of 3 Sv. Because

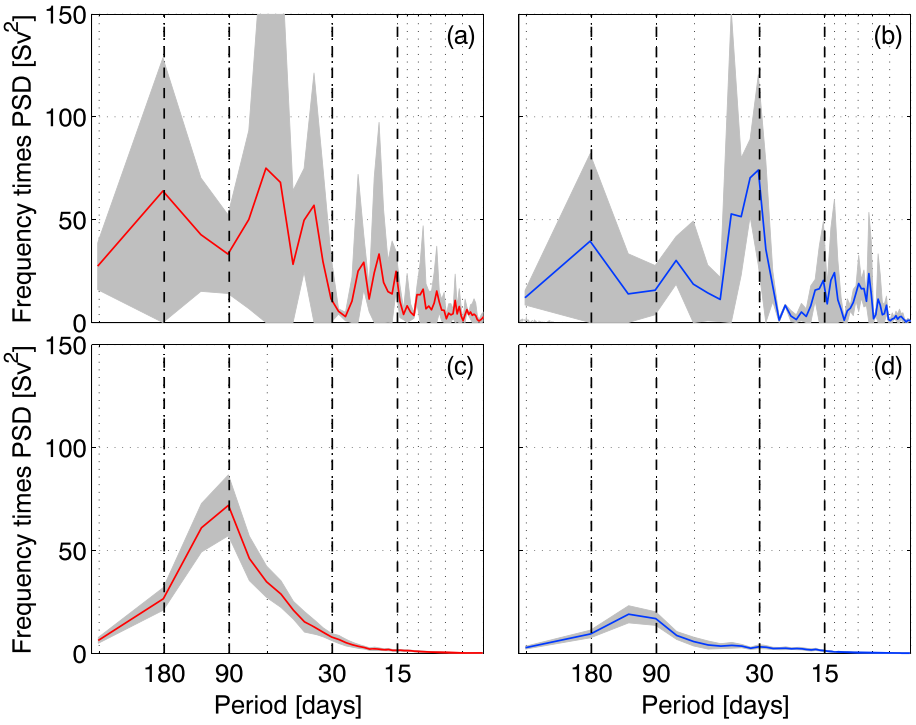

Figure 10. Variance preserving spectra of the Benguela Current (a) and the deep eastern boundary current (b) transport time series integrated in the regions shown in Figure 9. (c, d) Same as panels (a) and (b) calculated for the ocean general circulation model for the Earth simulator numerical model output for the full 36-year record. Gray shading indicates the 95% confidence limits based on the methods of Thomson and Emery (2014).

this range includes the observations-based estimate it can partially explain the larger 23-month mean DEBC in the observations.

Previous analysis of a shorter segment of the same OFES output has suggested that only ~22% of the lower MOC limb carried by the DWBC further north is crossing the South Atlantic near 20°S to feed the DEBC (Garzoli et al., 2015). Historical mean MOC estimates in the region have been defined as the maximum cumulative northward volume transport in the upper water column (e.g., Dong et al., 2014; Meinen et al., 2018). Based on these historical estimates at latitudes between 34°S and 35°S, which have yielded MOC estimates of 14.7 to 18.4 Sv, the lower MOC limb would feed roughly −3.2 to −4 Sv to the DEBC transport. The modeled DEBC mean transport value of −7 Sv found herein is much larger than this rough estimate. The actual observed DEBC mean volume transport is even larger than the model value, at −12 Sv. This mean value represents roughly 70% of the total MOC volume transport. It thus seems likely that a significant portion of the southward flow of NADW observed by the SAMBA-East CPIES is recirculating within the Cape Basin rather than participating directly in the MOC. This recirculation is also imposed by and/or controlled by the geographical features in the area. Specifically, the existence of the Walvis Ridge (Figure 1a) likely blocks most of the deep northward flow on the offshore part of the array. The presence of elevated dissolved oxygen values at the level of NADW, detailed in section 3.1 and Figure 7b, is additional arguments that support the idea of an interior branch recirculating in the basin.

The spectral analysis of the Benguela Current and the DEBC transport time series from the CPIES observations shows that the energy is generally higher in the transport record integrated in the upper part of the water column (Figure 10a) than in the transports in the lower part (Figure 10b) at all periods longer than 45 days. This comparison can be done as these spectra are plotted in variance-preserving form, and thus, the area under the curve is proportional to the energy at each period (e.g., Thomson & Emery, 2014). The most prominent spectral peaks for both time series are at time scales between 30 and 180 days. The 30-day period corresponds to the expected time scales associated with the propagation of Agulhas Rings, considering their sizes and propagation speeds. The 180-day time scale is characteristic of the upwelling time

Table 3
Distribution of Variance in the Benguela Current and the DEBC Transport From the CPIES Array

	Variance [Sv^2]		% of total variance	
Period band (days)	Benguela	DEBC	Benguela	DEBC
2–15	68	16	15	6
15–30	74	39	16	15
30–90	167	114	36	43
90–270 (semiannual)	120	61	26	23
>270	31	36	7	13

Note. CPIES = Current and Pressure recording Inverted Echo Sounders; DEBC = deep eastern boundary current.

scale in the South Benguela region (austral spring and summer; Blanke et al., 2005). Nevertheless, due to the relatively short record of the CPIES data (~2 years), caution must be stressed when interpreting variations at semiannual and longer time scales. The large error bars around the spectra at longer periods illustrate this point. A similar spectral analysis of the transports determined from the OFES output for the full 36-year record shows much narrower error bars around the resulting spectra (Figures 10c and 10d).

Another interesting result can be drawn from a comparison of the observed and modeled spectra. The modeled Benguela Current transport variability is weaker than the observed variability at all time scales except at around 90 days, where the model exhibits a single large energy peak that is not seen in the observations (Figures 10a and 10c). The modeled DEBC transport variability is much weaker than the observed transport variability at all time scales (Figures 10b and 10d). The model forcing fields are realistic, so a conclusion that can be drawn from the weaker spectra in the model is that the model is not doing a good job of moving the energy from the forcing fields down into the deeper reaches of the ocean at essentially all time scales that can be observed in the 23-month CPIES records. An earlier study by Dong et al. (2014) had shown that the models they tested were doing a poor job of moving energy down at the seasonal time scales, a result of artificially strong vertical density stratification, which prevented the models from moving energy down from the mixed layer to deeper levels. The results of the present study support this point and suggest further that this issue exists as well within the OFES model for time scales beyond seasonal.

Partitioning the observed variance into temporal bands (Table 3) shows that both the Benguela Current and the DEBC transport signals have 67% and 64%, respectively, of their variability at periods shorter than 90 days, which illustrates the necessity for high-frequency observations to avoid aliasing of these short-period variations into longer time scales. Previous observations focusing on coastal sea level anomalies along the west coast of South Africa showed that wind stress fluctuations could force poleward propagating coastally trapped waves (Schumann & Brink, 1990). Close to the location of our observations, these wave signals have a typical period of 8.5 days, right in the center of the 2- to 15-day period band where ~6–15% of the variance is observed (Table 3). Nevertheless, the largest fraction of the variance in both Benguela Current and DEBC transport time series is in the bands between 30 and 90 days, which corresponds to the expected time scales associated with the propagation of Agulhas Rings.

4. Conclusions

The SAMBA-East moored instruments provide the first direct continuous in situ EBCs observations spanning the Cape Basin between the Walvis Ridge and the coast along 34.5°S, yielding data over a 23-month period from September 2013 to July 2015. The CPIES-GEM data reveal the presence of the Benguela Current and a portion of the northward flowing Cape Peninsula Jet east of 11°E with a mean volume transport integrated from the surface to 1,270 dbar of 25 Sv and a daily standard deviation of 17 Sv (Figure 9). The estimated time-mean transports agree well with estimates from an Argo/altimetry synthesis and a XBT/WOA product (Table 2). However, the temporal standard deviation from the daily data from the moored CPIES exceeds that of the monthly Argo/altimetry synthesis and quarterly XBT/WOA product by roughly a factor of 3, demonstrating the high degree of variability observed at high frequencies that is not captured in the other data sets. The CPIES transports are also relatively similar to the 3-day output from a 36-year run of the OFES model, although the model transport variability appears to be artificially low. The time-average locations of the main water mass interfaces from the CPIES-GEM data confirm the presence of one of the upper limb MOC pathways (warm water route) passing through the Cape Basin. The largest variations in Benguela Current transport (peak-to-peak range of 124 Sv) appear to be associated mainly with the propagation of Agulhas Rings. West of P5 (11°E), the influence of these features is also revealed by altimetry, illustrating how the western edge of the Agulhas eddy corridor affects the mean flow of the transient component of the Benguela Current (Figure 6).

For the first time, the southward flowing DEBC, extending from the continental slope offshore to about 15°E, is observed with full-depth CPIES-GEM and bottom current meter data (Figure 4). The DEBC is surprisingly strong, with a mean value of −12 Sv, and it is highly variable (daily standard deviation of 17 Sv). The direct deep current meter measurements support the presence of this strong southward flow, as does the OFES model output—although the latter is artificially weak in the deep layer (compare Figures 4a and 5f). The two other ancillary data sets presented herein also provide hints of the DEBC adjacent to the continental slope as observed by the CPIES-GEM observations (Figures 5b and 5d); however, neither ancillary data set provides direct observations all the way to the bottom (Argo/altimetry synthesis ends at 2,000 dbar; XBT/WOA uses only climatology below ~800 m). The presence of recently ventilated NADW water from climatology and hydrographic sections at the location of the DEBC is consistent with a previous hypothesis about an interior pathway bringing waters from the DWBC over to the eastern boundary (Figure 7). The DEBC transport exhibits a large peak-to-peak range (115 Sv), linked to, among other things, the passage of Agulhas Rings and dipoles (Figure 9). The westward propagation characteristics observed across the array confirm that the observed deep propagation in the SAMBA-East region is dominated by the passage of Agulhas Rings. The deep circulation pattern is also influenced by recirculation cells.

The spectral analysis of the Benguela Current and DEBC transport time series reveals the predominant variability is at time scales between 30 and 90 days for both layers, consistent with the expected time scales associated with the propagation of Agulhas Rings (Figure 10). Despite evidence of specific events impacting both the Benguela Current and the DEBC transport time series, a systematic link between the two transport time series cannot be identified with a just under 2-year-long record. A smaller fraction of variance is also observed in the upper layer at time scales between 2 and 15 days, the characteristic of alongshore propagating waves, and a larger fraction around 180-day period, which is characteristic of the seasonal upwelling in the South Benguela Upwelling region. The relative short length of the observation records introduces large uncertainties at these longer time scales, and the model output cannot be used to provide guidance as weak lower layer transports suggest that the model is not allowing enough energy to penetrate to the deep ocean. This study demonstrates that daily observations are essential to successfully resolve the short time scale variability of the EBCs. From the historical mean MOC estimates and the percentage of this circulation feeding the DEBC, we can argue that a significant portion of the observed DEBC must be recirculating within the Cape Basin rather than participating in the MOC. Ongoing sustained observations along 34.5°S will allow us in the future to confirm or further assess the seasonal and interannual variabilities and determine the link between the upper and lower EBCs and their contribution to the MOC.

Appendix A: Temporal Stability of the GEM Field

A concern with the application of the GEM method, dating back to the original study where the method was created, was whether the averaging of data from different years/decades would mask long-period variability and/or trends (e.g., Meinen & Watts, 2000). There has always also been a question of the sensitivity of the resulting GEM lookup tables to the horizontal bounds of the region where data are used to build the fields. The new GEM fields created for the present study allow for the explicit evaluation of these issues. The first GEM lookup tables for the eastern boundary along 34.5°S were created by Meinen et al. (2013). These lookup tables were based on a data set of 123 CTD and 647 Argo profiles collected between 2009 and 2013 between 12°E and the South African continental shelf and between 37° and 31°S (Figure A1a). For the present study, updated GEM lookup tables were created using 378 CTD and 5,215 Argo profiles spanning a much wider time period from 1983 up to the present day (Figure A1b). The CTD/Argo data sets used for the new GEM fields span the same latitudinal range but a much larger zonal domain, from the continental shelf to 2°W (Figure A1b). The use of a much larger domain, in both space and time, allows for the comparison of the original and new GEM fields to determine the robustness of the relationships captured by the GEM fields. Inclusion of roughly seven times more profiles in building the GEM fields yields fairly similar lookup tables (cf. temperature lookup tables in Figures A1c and A1d).

A strength of the GEM method is that the scatter between the original data (CTD and Argo) and the resulting smoothed lookup tables provides a natural "accuracy estimate" for the GEM fields (e.g., Figures A1e and A1f). So the primary question in determining the robustness of the GEM field to changes to the spatial/temporal bounds of the hydrography is whether the differences between the GEM fields (Figures A1c and A1d) are larger than the scatter around the fields (Figures A1e and A1f; i.e., the

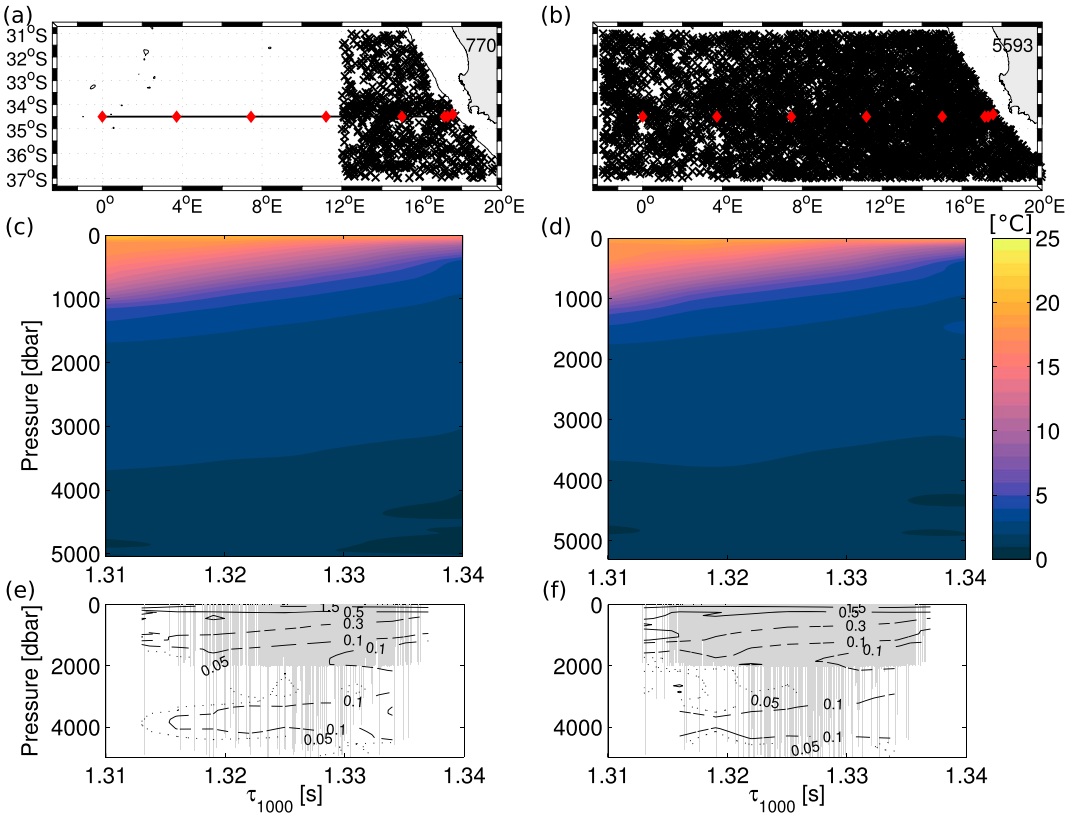

Figure A1. Left column, original gravest empirical mode (GEM) fields; right column, new GEM fields. (a, b) Positions of the conductivity-temperature-depth and Argo casts collected around the South Atlantic MOC Basin-Wide Array-East transect and used to create the GEM field. The Current and Pressure recording Inverted Echo Sounders locations are identified by the red diamonds along the transect. (c, d) GEM fields of temperature determined for the South Atlantic MOC Basin-Wide Array-East line. (e, f) The root mean square differences between the original hydrographic measurements and the GEM lookup table values. The solid, dashed, and dotted contours represent progressively smaller contour intervals, with values labeled in °C. The gray vertical lines show the locations of the hydrographic (conductivity-temperature-depth and Argo) measurements.

accuracy estimates). The root mean square differences between the original GEM field and the original CTD/Argo data range from about 1.5 °C at the surface (where seasonal variability is the maximum) down to around 0.05 °C in the deep ocean (Figure A1e). Adding more hydrographic casts yields better coverage of the τ parameter space and much higher sample numbers, but essentially the same accuracy for the GEM field (Figure A1f). The scatter around the salinity and density GEM fields is similarly about the same for the original and new GEM fields (not shown).

Figure A2 illustrates the differences between the original (black lines) and the updated GEM fields (colored lines) at two representative pressure levels (i.e., 500 dbar in the main thermocline and at 3,000 dbar in the deep ocean) using plots of temperature and salinity versus travel time. The updated GEM fields show weak warming and salinification relative to the older fields at 500 and 3,000 dbar; however, the updated GEM estimates remain for both variables and pressure levels within the accuracy of the original GEM fields, and so are not statistically different. For the density GEM fields (not shown), the results are quite similar. This comparison demonstrates that to within the accuracy of the technique, the GEM fields are temporally stable (at least over the past ~35 years). Furthermore, the comparison also indicates that the GEM fields are not strongly sensitive to the longitudes of the hydrography bounding box.

Appendix B: Benguela Current and DEBC Transports Accuracy Estimates

The transport accuracy estimates for the flows across the SAMBA-East transect have been derived following a classical "first principles" ideal, specifically paralleling the methods described within the appendix of Meinen et al. (2013). Following this technique, we have separated the sources of error in the transport as being random or biases in relation to time variability (Table B1). In this study, all the errors are calculated

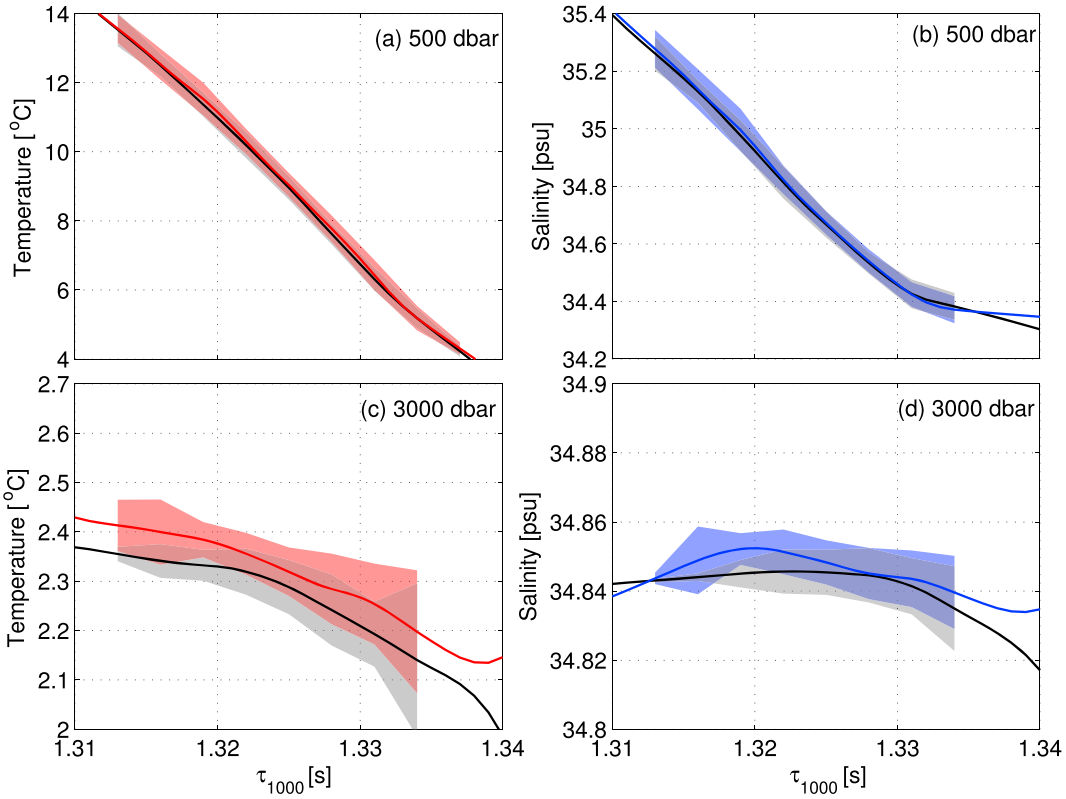

Figure A2. Temperature (a, c) and salinity (b, d) function of the travel time at 1,000 dbar for the original gravest empirical mode (GEM) fields (black lines) and the updated GEM fields (colored lines) at 500 and 3,000 dbar. The shaded areas represent the root mean square scatter between the original hydrographic measurements and the GEM lookup table values.

separately for the Benguela Current and the DEBC transports. Random sources of errors (i.e., those sources that are independent of one another) are combined via a standard square root of the sum of squares method. A detailed explanation of the sources of error can be found in Meinen et al. (2013); here only a brief discussion is presented, focusing primarily on the specifics of this application.

Table B1
Estimates of the Error Contributions to the Benguela Current and DEBC Transport Accuracies

	Accuracy estimate	
Random sources	Benguela	DEBC
Measured τ accuracy	1.7 Sv	1.8 Sv
Scatter in τ PIES versus τ 1,000	2 Sv	2.5 Sv
GEM lookup table accuracy	4.5 Sv	3.6 Sv
Baroclinic shear	1.1 Sv	4.7 Sv
Measured pressure accuracy	2.1 Sv	4.5 Sv
Total random	5.8 Sv	8.1 Sv
Bias Sources	Benguela	DEBC
Calibration of τ PIES with concurrent CTDs	1.7 Sv	1.8 Sv
Accuracy of reference velocity time-mean	2.8 Sv	2.2 Sv
Total bias	3.3 Sv	2.8 Sv

Note. PIES = pressure-equipped inverted echo sounder; DEBC = deep eastern boundary current; GEM = gravest empirical mode; CTD = conductivity-temperature-depth.

As described by Meinen et al. (2013), there are several accuracy limitations to the travel times of the PIES/CPIES. To convert the different travel time (τ) based accuracies into equivalent transport accuracies, a linear relationship between the vertical integral of the dynamic height anomaly (i.e., the baroclinic streamfunction, also sometimes called the Fofonoff Potential,χ) and τ was used. The vertical integration domain for the Fofonoff potential was selected to be consistent with the vertical boundaries used for the transport integrals themselves, that is, between the surface and 1,270 dbar (χ^0_{1270}) for the Benguela Current and between 1,270 and 4,050 dbar for the DEBC (χ^{1270}_{4050}). The tight relationship between τ and χ for both parts of the water column is evident (Figure B1). The slope of the linear fit (Figure B1, red lines) between these quantities is equal to -2.0×10^5 J/m^2/ms for the upper part and -2.1×10^5 J/m^2/msec for the lower part. The resulting χ-based accuracy estimates were then converted into transport errors assuming a constant density of 1,030 kg/m^3 and the appropriate local Coriolis parameter. As the transport here is based on geostrophic estimates, the errors are considered at/between sites P1 and P5 for the Benguela Current and at/between sites P1 and P4 for the DEBC.

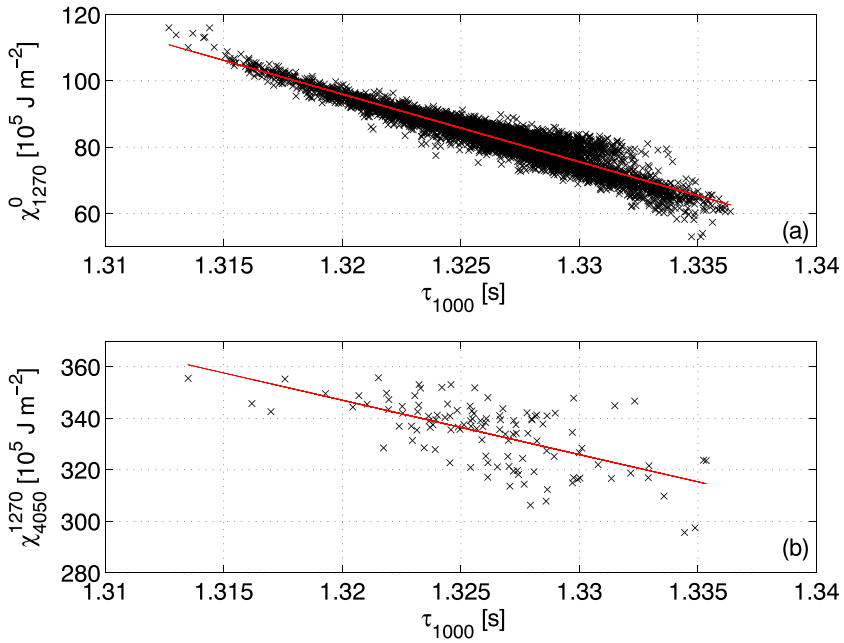

Figure B1. Scatter plot illustrating the relationship between the travel time at 1,000 dbar and the Fofonoff potential for the upper part (χ^0_{1270}) and lower part (χ^{1270}_{4050}) of the water column.

The random accuracy of the geostrophic velocity (or transport) relative to an assumed level of no motion is a function of four terms: (1) the accuracy of measured travel time (τ) from the instrument (0.5 ms; Donohue et al., 2010); (2) the scatter in the calibration relationship that converted τ at the depth of the CPIES into the equivalent τ at 1,000 dbar; (3) the accuracy of the GEM lookup tables; and (4) the scatter introduced by projecting the τ at 1,000 dbar (and their derived dynamic height profiles) downward using the GEM lookup tables to the deepest vertical integration boundary (1,270 dbar for the Benguela Current and 4,050 dbar for the DEBC). In addition to these four terms, an additional random source in the final absolute geostrophic velocities (transports) is the accuracy of the pressure gauges (0.01 dbar; Donohue et al., 2010), which impacts the accuracy of the reference velocity.

All these errors were estimated following the methods shown in Meinen et al. (2013) except for the accuracy of the GEM lookup tables (3) for the DEBC. According to the prior study, this accuracy would be estimated as the root mean square scatter in the relationship between τ and χ^{1270}_{4050} (Figure B1b). However, the number of hydrographic casts reaching down to a pressure of 4,050 dbar is far too limited (only 116 casts) to estimate the accuracy with this method. Here we instead estimated an accuracy based on the accuracy derived for the upper water column value rescaled by a value proportional to the area size of the DEBC integration domain versus the area size of the Benguela Current integration domain (733 km^2, upper integration domain area; 590 km^2, lower integration domain area).

When all of the sources of random errors are combined, we find total random errors of 5.8 Sv for the daily Benguela Current transport estimates and 8.1 Sv for the daily DEBC transport estimates (Table B1).

In addition to random errors affecting the time variability of the transport, some errors can affect the time-mean transport (e.g., biases). Following the methods presented in Meinen et al. (2013), two potential sources of bias were considered in this study: (1) the mean offset/calibration of the CPIES measured τ into the equivalent τ at 1,000 dbar (as opposed to the random scatter about that relationship, which relates to one of the random error methods above) and (2) the accuracy of the applied time-mean reference velocity. The former error component is estimated to be about 0.5 ms, which corresponds to a transport accuracy of 1.7/1.8 Sv for the Benguela Current/DEBC. The latter bias source is much harder to quantify of course —as the primary data set used is a numerical model. For this analysis, the reference velocity accuracy was estimated here as the difference between the time-mean transbasin-averaged velocity at the reference level from the 36-year OFES run and the time-mean transbasin-averaged velocity at that same level from the

Argo/altimetry synthesis discussed in the text (0.004 m/s). The sources of bias are assumed to be as independent of one another, so they can also be combined via a square root of the sum of squares method, yielding 3.3 and 2.8 Sv as the potential bias error in the time-mean Benguela Current and DEBC transports, respectively (Table B1).

Acknowledgments
The authors would like to express their great appreciation to the Captain, officers, and crew of the RV SA Agulhas II, who have supported this program to date. We are also very grateful to the technical staff who worked on the preparation, deployment, and the recovery of the instruments, and our thanks to those who have helped coordinate these challenging international cruise collaborations. M. K., M. L. H., S. G., and S. M. were supported in part under the auspices of the Cooperative Institute for Marine and Atmospheric Studies (CIMAS), a cooperative institute of the University of Miami and NOAA, cooperative agreement NA10OAR4320143. M. K., M. L. H., and R. P. acknowledge support from the NOAA Climate Variability Program (GC16-212 and NA13OAR4310131) and NASA (Grant NNX14AH60G). C. M., C. S., R. P., and S. D. were supported by NOAA's Ocean Observing and Monitoring Division (FundRef 100007298). The Miami authors all also acknowledge additional support from the NOAA Atlantic Oceanographic and Meteorological Laboratory. S. S. and T. T. acknowledge support from the 11-ANR-56-004 SAMOC Research Project. S. S. also received support from the European Union Horizon 2020 Research and Innovation Programme under grant 633211 (AtlantOS). IA, M. v. d. B., and T. L. acknowledge support from the DST-NRF-SANAP Programme and the South African DEA. Users can access the CPIES data from the SAMOC initiative web page (aoml.noaa.gov/phod/SAMOC_international/samoc_data.php). Data from the hydrographic casts are being uploaded to the "Marine Information Management System" (data.ocean.gov.za/). The Argo/altimetry synthesis and the XBT/WOA products can be obtained from the AOML/PhOD website (respectively, www.aoml.noaa.gov/phod/samoc_argo_altimetry/data.php; www.aoml.noaa.gov/phod/goos/xbtscience/data.php). The altimeter products were developed by SSALTO/DUACS and distributed by AVISO, with support from CNES (www.aviso.oceanobs.com/duacs/). The Mesoscale Eddy Trajectory Atlas Product was produced by SSALTO/DUACS and distributed by AVISO+ (aviso.altimetry.fr/) with support from CNES, in collaboration with Oregon State University with support from NASA. Argo data were collected and made freely available by the Coriolis Project and Programmes that contribute to it (coriolis.eu.org). The OFES outputs were provided by Asia-Pacific Data Research Center,

References

Ansorge, I. J., Baringer, M. O., Campos, E. J. D., Dong, S., Fine, R. A., Garzoli, S. L., et al. (2014). Basin-wide oceanographic array bridges the South Atlantic. *Eos, Transactions American Geophysical Union*, *95*(6), 53–54. https://doi.org/10.1002/2014EO060001

Ansorge, I. J., Speich, S., Lutjeharms, J. R. E., Goni, G. J., Rautenbach, C. D. W., Froneman, P. W., et al. (2005). Monitoring the oceanic flow between Africa and Antarctica: Report of the first GoodHope cruise: Research in action. *South African Journal of Science*, *101*(1–2), 29–35.

Arhan, M., Mercier, H., & Park, Y. H. (2003). On the deep water circulation of the eastern South Atlantic Ocean. *Deep Sea Research, Part I*, *50*(7), 889–916. https://doi.org/10.1016/S0967-0637(03)00072-4

Baker-Yeboah, S., Byrne, D. A., & Watts, D. R. (2010). Observations of mesoscale eddies in the South Atlantic Cape Basin: Baroclinic and deep barotropic eddy variability. *Journal of Geophysical Research*, *115*, C12069. https://doi.org/10.1029/2010JC006236

Baker-Yeboah, S., Watts, D. R., & Byrne, D. A. (2009). Measurements of sea surface height variability in the eastern South Atlantic from pressure sensor-equipped inverted echo sounders: Baroclinic and barotropic components. *Journal of Atmospheric and Oceanic Technology*, *26*(12), 2593–2609. https://doi.org/10.1175/2009JTECHO659.1

Bang, N. D., & Andrews, W. R. H. (1974). Direct current measurements of an oceanic frontal jet in the upwelling regime west of Cape Town. *Journal of Marine Research*, *32*, 405–417.

Beal, L. M. (2009). A time series of Agulhas undercurrent transport. *Journal of Physical Oceanography*, *39*(10), 2436–2450. https://doi.org/10.1175/2009JPO4195.1

Beal, L. M., Elipot, S., Houk, A., & Leber, G. M. (2015). Capturing the transport variability of a western boundary jet: Results from the Agulhas current time-series experiment (ACT). *Journal of Physical Oceanography*, *45*(5), 1302–1324. https://doi.org/10.1175/JPO-D-14-0119.1

Biastoch, A., Beal, L. M., Lutjeharms, J. R. E., & Casal, T. G. D. (2009). Variability and coherence of the Agulhas undercurrent in a high-resolution ocean general circulation model. *Journal of Physical Oceanography*, *39*(10), 2417–2435. https://doi.org/10.1175/2009JPO4184.1

Biastoch, A., Böning, C. W., & Lutjeharms, J. R. E. (2008). Agulhas leakage dynamics affects decadal variability in Atlantic overturning circulation. *Nature*, *456*(7221), 489–492. https://doi.org/10.1038/nature07426

Biastoch, A., Durgadoo, J. V., Morrison, A. K., Van Sebille, E., Weijer, W., & Griffies, S. M. (2015). Atlantic multi-decadal oscillation covaries with Agulhas leakage. *Nature*, *6*(1), 10,082. https://doi.org/10.1038/ncomms10082

Biastoch, A., Sein, D., Durgadoo, J. V., Wang, Q., & Danilov, S. (2018). Simulating the Agulhas system in global ocean models-nesting vs. multi-resolution unstructured meshes. *Ocean Modelling*, *121*, 117–131. https://doi.org/10.1016/j.ocemod.2017.12.002

Bingham, R. J., Hughes, C. W., Roussenov, V., & Williams, R. G. (2007). Meridional coherence of the North Atlantic meridional overturning circulation. *Geophysical Research Letters*, *34*, L23606. https://doi.org/10.1029/2007GL031731

Blanke, B., Speich, S., Bentamy, A., Roy, C., & Sow, B. (2005). Modeling the structure and variability of the southern Benguela upwelling using QuikSCAT wind forcing. *Journal of Geophysical Research*, *110*, C07018. https://doi.org/10.1029/2004JC002529

Bower, A. S., Lozier, M. S., Gary, S. F., & Böning, C. W. (2009). Interior pathways of the North Atlantic meridional overturning circulation. *Nature*, *459*(7244), 243–247. https://doi.org/10.1038/nature07979

Boyd, A. J., & Nelson, G. (1998). Variability of the Benguela current off the cape Peninsula, South Africa. *African Journal of Marine Science*, *19*(1), 27–39. https://doi.org/10.2989/025776198784126665

Boyer, T. P., Antonov, J. I., Baranova, O. K., Coleman, C., Garcia, H. E., Grodsky, A., et al. (2013). World Ocean Database 2013. In S. Levitus & A. Mishonov (Eds.), *NOAA Atlas NESDIS 72* (p. 209). MD: Silver Spring. https://doi.org/10.7289/V5NZ85MT

Bryden, H. L., Beal, L. M., & Duncan, L. M. (2005). Structure and transport of the Agulhas current and its temporal variability. *Journal of Oceanography*, *61*(3), 479–492. https://doi.org/10.1007/s10872-005-0057-8

Buckley, M. W., & Marshall, J. (2016). Observations, inferences, and mechanisms of the Atlantic meridional overturning circulation: A review. *Reviews of Geophysics*, *54*, 5–63. https://doi.org/10.1002/2015RG000493

Byrne, D. A., Gordon, A. L., & Haxby, W. F. (1995). Agulhas eddies: A synoptic view using Geosat ERM data. *Journal of Physical Oceanography*, *25*(5), 902–917. https://doi.org/10.1175/1520-0485(1995)025<0902:AEASVU>2.0.CO;2

Chelton, D. B., Schlax, M. G., & Samelson, R. M. (2011). Global observations of nonlinear mesoscale eddies. *Progress in Oceanography*, *91*(2), 167–216. https://doi.org/10.1016/j.pocean.2011.01.002

Chereskin, T. K., Donohue, K. A., Watts, D. R., Tracey, K. L., Firing, Y. L., & Cutting, A. L. (2009). Strong bottom currents and cyclogenesis in Drake Passage. *Geophysical Research Letters*, *36*, L23602. https://doi.org/10.1029/2009GL040940

de Ruijter, W. P. M., Biastoch, A., Drijfhout, S. S., Lutjeharms, J. R. E., Matano, R. P., Pichevin, T., et al. (1999). Indian-Atlantic interocean exchange: Dynamics, estimation and impact. *Journal of Geophysical Research*, *104*(C9), 20,885–20,910. https://doi.org/10.1029/1998JC900099

Dencausse, G., Arhan, M., & Speich, S. (2010). Routes of Agulhas rings in the southeastern Cape Basin. *Deep Sea Research, Part I*, *57*(11), 1406–1421. https://doi.org/10.1016/j.dsr.2010.07.008

Dengler, M., Schott, F. A., Eden, C., Brandt, P., Fischer, J., & Zantopp, R. J. (2004). Break-up of the Atlantic Deep Western Boundary Current into eddies at 8 S. *Nature*, *432*(7020), 1018–1020. https://doi.org/10.1038/nature03134

Dijkstra, H. A. (2007). Characterization of the multiple equilibria regime in a global ocean model. *Tellus A*, *59*(5), 695–705. https://doi.org/10.1111/j.1600-0870.2007.00267.x

Dong, S., Baringer, M. O., Goni, G. J., Meinen, C. S., & Garzoli, S. L. (2014). Seasonal variations in the South Atlantic meridional overturning circulation from observations and numerical models. *Geophysical Research Letters*, *41*, 4611–4618. https://doi.org/10.1002/2014GL060428

Dong, S., Garzoli, S., & Baringer, M. (2011). The role of interocean exchanges on decadal variations of the meridional heat transport in the South Atlantic. *Journal of Physical Oceanography*, *41*(8), 1498–1511. https://doi.org/10.1175/2011JPO4549.1

which is a part of the International Pacific Research Center at the University of Hawai'i at Mānoa, funded in part by the National Oceanic and Atmospheric Administration (NOAA). The authors received several helpful suggestions for improving an earlier version of this manuscript from Hally B. Stone and two anonymous reviewers, and their help is gratefully noted.

Dong, S., Garzoli, S., Baringer, M., Meinen, C., & Goni, G. (2009). Interannual variations in the Atlantic meridional overturning circulation and its relationship with the net northward heat transport in the South Atlantic. *Geophysical Research Letters*, *36*, L20606. https://doi.org/10.1029/2009GL039356

Dong, S., Goni, G., & Bringas, F. (2015). Temporal variability of the South Atlantic meridional overturning circulation between 20°S and 35°S. *Geophysical Research Letters*, *42*, 7655–7662. https://doi.org/10.1002/2015GL065603

Donohue, K. A., Tracey, K. L., Watts, D. R., Chidichimo, M. P., & Chereskin, T. K. (2016). Mean Antarctic circumpolar current transport measured in Drake Passage. *Geophysical Research Letters*, *43*, 11,760–11,767. https://doi.org/10.1002/2016GL070319

Donohue, K. A., Watts, D. R., Tracey, K. L., Greene, A. D., & Kennelly, M. (2010). Mapping circulation in the Kuroshio extension with an array of current and pressure recording inverted echo sounders. *Journal of Atmospheric and Oceanic Technology*, *27*, 507–527. https://doi.org/10.1175/2009JTECHO686.1

Drijfhout, S. S., Weber, S. L., & van der Swaluw, E. (2011). The stability of the MOC as diagnosed from model projections for pre-industrial, present and future climates. *Climate Dynamics*, *37*(7–8), 1575–1586. https://doi.org/10.1007/s00382-010-0930-z

Duncombe Rae, C. D. (2005). A demonstration of the hydrographic partition of the Benguela upwelling ecosystem at 26°40′S. *African Journal of Marine Science*, *27*(3), 617–628. https://doi.org/10.2989/18142320509504122

Duncombe Rae, C. M., Garzoli, S. L., & Gordon, A. L. (1996). The eddy field of the Southeast Atlantic Ocean: A statistical census from the Benguela sources and transports project. *Journal of Geophysical Research*, *101*(C5), 11,949–11,964. https://doi.org/10.1029/95JC03360

Fennel, W. (1999). Theory of the Benguela upwelling system. *Journal of Physical Oceanography*, *29*(2), 177–190. https://doi.org/1520-0485(1999)029<0177:TOTBUS>2.0.CO;2

Ganachaud, A. (2003). Large-scale mass transports, water mass formation, and diffusivities estimated from World Ocean Circulation Experiment (WOCE) hydrographic data. *Journal of Geophysical Research*, *108*(C7). https://doi.org/10.1029/2002JC001565

Garcia, H. E., Locarnini, R. A., Boyer, T. P, Antonov, J. I., Baranova, O. K., Zweng, M. M., et al. (2014). World Ocean Atlas 2013, volume 3: Dissolved oxygen, apparent oxygen utilization, and oxygen saturation. S. Levitus, Ed., A. Mishonov technical Ed.; NOAA atlas NESDIS 75, 27.

Garzoli, S. L. (1993). Geostrophic velocity and transport variability in the Brazil-Malvinas confluence. *Deep Sea Research, Part I*, *40*(7), 1379–1403. https://doi.org/10.1016/0967-0637(93)90118-M

Garzoli, S. L., & Baringer, M. O. (2007). Meridional heat transport determined with expandable bathythermographs—Part II: South Atlantic transport. *Deep-Sea Research Part I*, *54*(8), 1402–1420. https://doi.org/10.1016/j.dsr.2007.04.013

Garzoli, S. L., Baringer, M. O., Dong, S., Perez, R. C., & Yao, Q. (2013). South Atlantic meridional fluxes. *Deep-Sea Research Part I*, *71*, 21–32. https://doi.org/10.1016/j.dsr.2012.09.003

Garzoli, S. L., Dong, S., Fine, R., Meinen, C. S., Perez, R. C., Schmid, C., et al. (2015). The fate of the Deep Western Boundary Current in the South Atlantic. *Deep Sea Research, Part I*, *103*, 125–136. https://doi.org/10.1016/j.dsr.2015.05.008

Garzoli, S. L., Goni, G. J., Mariano, A. J., & Olson, D. B. (1997). Monitoring the upper southeastern Atlantic transports using altimeter data. *Journal of Marine Research*, *55*(3), 453–481. https://doi.org/10.1357/0022240973224355

Garzoli, S. L., & Gordon, A. L. (1996). Origins and variability of the Benguela current. *Journal of Geophysical Research*, *101*(C1), 897–906. https://doi.org/10.1029/95JC03221

Garzoli, S. L., & Matano, R. (2011). The South Atlantic and the Atlantic meridional overturning circulation. *Deep Sea Research, Part II*, *58*(17-18), 1837–1847. https://doi.org/10.1016/j.dsr2.2010.10.063

Gladyshev, S., Arhan, M., Sokov, A., & Speich, S. (2008). A hydrographic section from South Africa to the southern limit of the Antarctic circumpolar current at the Greenwich meridian. *Deep Sea Research, Part I*, *55*(10), 1284–1303. https://doi.org/10.1016/j.dsr.2008.05.009

Goes, M., Goni, G., & Dong, S. (2015). An optimal XBT-based monitoring system for the South Atlantic meridional overturning circulation at 34° S. *Journal of Geophysical Research: Ocean*, *120*, 161–181. https://doi.org/10.1002/2014JC010202

Goni, G. J., Garzoli, S. L., Roubicek, A. J., Olson, D. B., & Brown, O. B. (1997). Agulhas ring dynamics from TOPEX/POSEIDON satellite altimeter data. *Journal of Marine Research*, *55*(5), 861–883. https://doi.org/10.1357/0022240973224175

Goni, G. J., & Johns, W. E. (2003). Synoptic study of warm rings in the North Brazil current retroflection region using satellite altimetry. *Elsevier Oceanography Series*, *68*, 335–356. https://doi.org/10.1016/S0422-9894(03)80153-8

Gordon, A. L. (1986). Interocean exchange of thermocline water. *Journal of Geophysical Research*, *91*(C4), 5037–5046. https://doi.org/10.1029/JC091iC04p05037

Gordon, A. L., Weiss, R. F., Smethie, W. M., & Warner, M. J. (1992). Thermocline and intermediate water communication between the South Atlantic and Indian oceans. *Journal of Geophysical Research*, *97*(C5), 7223–7240. https://doi.org/10.1029/92JC00485

Herrford, J., Brandt, P., & Zenk, W. (2017). Property changes of deep and bottom waters in the Western Tropical Atlantic. *Deep Sea Research, Part I*, *124*, 103–125. https://doi.org/10.1016/j.dsr.2017.04.007

Heywood, K. J., & King, B. A. (2002). Water masses and baroclinic transports in the South Atlantic and Southern oceans. *Journal of Marine Research*, *60*(5), 639–676. https://doi.org/10.1357/002224002762688687

Hogg, N. G., & Johns, W. E. (1995). Western boundary currents. *Reviews of Geophysics*, *33*(S2), 1311–1334. https://doi.org/10.1029/95RG00491

Huisman, S. E., DenToom, M., Dijkstra, H. A., & Drijfhout, S. (2010). An indicator of the multiple equilibria regime of the Atlantic meridional overturning circulation. *Journal of Physical Oceanography*, *40*(3), 551–567. https://doi.org/10.1175/2009JPO4215.1

Hummels, R., Brandt, P., Dengler, M., Fischer, J., Araujo, M., Veleda, D., & Durgadoo, J. V. (2015). Interannual to decadal changes in the western boundary circulation in the Atlantic at 11°S. *Geophysical Research Letters*, *42*, 7615–7622. https://doi.org/10.1002/2015GL065254

Illig, S., Bachèlery, M. L., & Cadier, E. (2018). Subseasonal coastal trapped wave propagations in the Southeastern Pacific and Atlantic oceans: 2. Wave Characteristics and Connection With Equatorial Variability. *Journal of Geophysical Research: Oceans*, *123*, 3942–3961. https://doi.org/10.1029/2017JC013540

Kersalé, M., Lamont, T., Speich, S., Terre, T., Laxenaire, R., Roberts, M. J., et al. (2018). Moored observations of mesoscale features in the Cape Basin: Characteristics and local impacts on water mass distributions. *Ocean Science*, *14*(5), 923–945. https://doi.org/10.5194/os-14-923-2018

Koltermann, K. P., Gouretski, V., & Jancke, K. (2011). Hydrographic Atlas of the World Ocean Circulation Experiment (WOCE). In M. Sparrow, P. Chapman, & J. Gould (Eds.), *Volume 3: Atlantic ocean* (221 pp.). Southampton, UK: International WOCE Project Office. ISBN 090417557X

Kopte, R., Brandt, P., Dengler, M., Tchipalanga, P. C. M., Macuéria, M., & Ostrowski, M. (2017). The Angola current: Flow and hydrographic characteristics as observed at 11°S. *Journal of Geophysical Research: Oceans*, *122*, 1177–1189. https://doi.org/10.1002/2016JC012374

Lass, H. U., & Mohrholz, V. (2008). On the interaction between the subtropical gyre and the subtropical cell on the shelf of the SE Atlantic. *Journal of Marine Systems*, *74*(1–2), 1–43. https://doi.org/10.1016/j.jmarsys.2007.09.008

Lopez, H., Goni, G., & Dong, S. (2017). A reconstructed South Atlantic meridional overturning circulation time series since 1870. *Geophysical Research Letters*, *44*, 3309–3318. https://doi.org/10.1002/2017GL073227

Lozier, M. S. (2010). Deconstructing the conveyor belt. *Science*, *328*(5985), 1507–1511. https://doi.org/10.1126/science.1189250

Lumpkin, R., & Speer, K. (2007). Global ocean meridional overturning. *Journal of Physical Oceanography*, *37*(10), 2550–2562. https://doi.org/10.1175/JPO3130.1

Lutjeharms, J. R. E. (2006). *The Agulhas current* (p. 329). Berlin, Heidelberg: Springer. https://doi.org/10.1007/3-540-37212-1

Lutjeharms, J. R. E., Boebel, O., & Rossby, T. (1997). KAPEX: An international experiment to study deep water movement around southern Africa. *South African Journal of Science*, *93*, 377–381.

Lutjeharms, J. R. E., & Cooper, J. (1996). Interbasin leakage through Agulhas current filaments. *Deep Sea Research, Part I*, *43*(2), 213–215,238. https://doi.org/10.1016/0967-0637(96)00002-7

Majumder, S., & Schmid, C. (2018). A study of the variability in the Benguela current volume transport. *Ocean Science*, *14*(2), 273–283. https://doi.org/10.5194/os-14-273-2018

Majumder, S., Schmid, C., & Halliwell, G. (2016). An observations and model-based analysis of meridional transports in the South Atlantic. *Journal of Geophysical Research: Oceans*, *121*, 5622–5638. https://doi.org/10.1002/2016JC011693

Masumoto, Y., Sasaki, H., Kagimoto, T., Komori, N., Ishida, A., Sasai, Y., et al. (2004). A fifty-year eddy-resolving simulation of the world ocean: Preliminary outcomes of OFES (OGCM for the Earth Simulator). *Journal of the Earth Simulator*, *1*, 35–56.

Meinen, C. S., Garzoli, S. L., Johns, W. E., & Baringer, M. O. (2004). Transport variability of the Deep Western Boundary Current and the Antilles current off Abaco Island, Bahamas. *Deep Sea Research, Part I*, *51*(11), 1397–1415. https://doi.org/10.1016/j.dsr.2004.07.007

Meinen, C. S., Garzoli, S. L., Perez, R. C., Campos, E., Piola, A. R., Chidichimo, M. P., et al. (2017). Characteristics and causes of Deep Western Boundary Current transport variability at 34.5°S during 2009-2014. *Ocean Science*, *13*(1), 175. https://doi.org/10.5194/os-13-175-2017

Meinen, C. S., Luther, D. S., & Baringer, M. O. (2009). Structure, transport and potential vorticity of the Gulf Stream at 68°W: Revisiting older data sets with new techniques. *Deep Sea Research, Part I*, *56*(1), 41–60. https://doi.org/10.1016/j.dsr.2008.07.010

Meinen, C. S., Speich, S., Perez, R. C., Dong, S., Piola, A. R., Garzoli, S. L., et al. (2013). Temporal variability of the meridional overturning circulation at 34.5°S: Results from two pilot boundary arrays in the South Atlantic. *Journal of Geophysical Research: Ocean*, *118*, 6461–6478. https://doi.org/10.1002/2013JC009228

Meinen, C. S., Speich, S., Piola, A. R., Ansorge, I. J., Campos, E. J. D., Kersalé, M., et al. (2018). Meridional overturning circulation transport variability at 34.5°S during 2009–2017: Baroclinic and barotropic flows and the dueling influence of the boundaries. *Geophysical Research Letters*, *45*, 4180–4188. https://doi.org/10.1029/2018GL077408

Meinen, C. S., & Watts, D. R. (1998). Calibrating inverted echo sounders equipped with pressure sensors. *Journal of Atmospheric and Oceanic Technology*, *15*(6), 1339–1345. https://doi.org/10.1175/1520-0426(1998)015<1339:CIESEW>2.0.CO;2

Meinen, C. S., & Watts, D. R. (2000). Vertical structure and transport on a transect across the North Atlantic current near 42°N: Time series and mean. *Journal of Geophysical Research*, *105*(C9), 21,869–21,891. https://doi.org/10.1029/2000JC900097

Mooers, C. N. K., Meinen, C. S., Baringer, M. O., Bang, I., Rhodes, R., Barron, C. N., & Bub, F. (2005). Cross validating ocean prediction and monitoring systems. *Eos, Transactions American Geophysical Union*, *86*(29), 269), 272–273. https://doi.org/10.1029/2005EO290002

Munk, W. H., & Cartwright, D. E. (1966). Tidal spectroscopy and prediction. *Philosophical Transactions. Royal Society of London*, *259*(1105), 533–581. https://doi.org/10.1098/rsta.1966.0024

Nelson, G. (1989). Poleward motion in the Benguela area. In *Poleward flows along eastern ocean boundaries* (pp. 110–130). New York: Springer.

Oliveira, F. S., & Polito, P. S. (2013). Characterization of westward propagating signals in the South Atlantic from altimeter and radiometer records. *Remote Sensing of Environment*, *134*, 367–376. https://doi.org/10.1016/j.rse.2013.03.019

Olson, D. B., & Evans, R. H. (1986). Rings of the Agulhas current. *Deep Sea Research, Part I*, *33*(1), 27–42. https://doi.org/10.1016/0198-0149(86)90106-8

Palma, E. D., & Matano, R. P. (2017). South Atlantic circulation and variability from a data assimilating model. In *Marine pollution and climate change* (pp. 39–65). CRC Press.

Perez, R. C., Baringer, M. O., Dong, S., Garzoli, S. L., Goes, M., Goni, G. J., et al. (2015). Measuring the Atlantic meridional overturning circulation. *Marine Technology Society Journal*, *49*(2), 167–177. https://doi.org/10.4031/MTSJ.49.2.14

Perez, R. C., Garzoli, S. L., Meinen, C. S., & Matano, R. P. (2011). Geostrophic velocity measurement techniques for the meridional overturning circulation and meridional heat transport in the South Atlantic. *Journal of Atmospheric and Oceanic Technology*, *28*(11), 1504–1521. https://doi.org/10.1175/JTECH-D-11-00058.1

Peterson, R. G., & Stramma, L. (1991). Upper-level circulation in the South Atlantic Ocean. *Progress in Oceanography*, *26*(1), 1–73. https://doi.org/10.1016/0079-6611(91)90006-8

Pond, S., & Pickard, G. L. (1983). *Introductory dynamical oceanography* (2nd ed., p. 329). Pergamon, Oxford.

Purkey, S. G., & Johnson, G. C. (2010). Warming of global abyssal and deep Southern Ocean between the 1990s and the 2000s: Contributions to global heat and sea level rise budgets. *Journal of Climate*, *23*(23), 6336–6351. https://doi.org/10.1175/2010JCLI3682.1

Rahmstorf, S., Feulner, G., Mann, M. E., Robinson, A., Rutherford, S., & Schaffernicht, E. J. (2015). Exceptional twentieth-century slowdown in Atlantic Ocean overturning circulation. *Nature Climate Change*, *5*(5), 475–480. https://doi.org/10.1038/nclimate2554

Richardson, P. L., Lutjeharms, J. R. E., & Boebel, O. (2003). Introduction to the "inter-ocean exchange around southern Africa". *Deep Sea Research, Part I*, *50*(1), 1–12. https://doi.org/10.1016/S0967-0645(02)00376-4

Rimaud, J., Speich, S., Blanke, B., & Grima, N. (2012). The exchange of Intermediate Water in the southeast Atlantic: Water mass transformations diagnosed from the Lagrangian analysis of a regional ocean model. *Journal of Geophysical Research*, *117*, C08034. https://doi.org/10.1029/2012JC008059

Rintoul, S. R. (1991). South Atlantic interbasin exchange. *Journal of Geophysical Research*, *96*(C2), 2675–2692. https://doi.org/10.1029/90JC02422

Rio, M. H., Mulet, S., & Picot, N. (2014). Beyond GOCE for the ocean circulation estimate: Synergetic use of altimetry, gravimetry, and in situ data provides new insight into geostrophic and Ekman currents. *Geophysical Research Letters*, *41*, 8918–8925. https://doi.org/10.1002/2014GL061773

Rossby, T. (1969). On monitoring depth variations of the main thermocline acoustically. *Journal of Geophysical Research*, *74*, 5542–5546. https://doi.org/10.1029/JC074i023p05542

Rusciano, E., Speich, S., & Ollitrault, M. (2012). Interocean exchanges and the spreading of Antarctic Intermediate Water south of Africa. *Journal of Geophysical Research*, *117*, C10010. https://doi.org/10.1029/2012JC008266

Sasaki, H., Nonaka, M., Masumoto, Y., Sasai, Y., Uehara, H., & Sakuma, H. (2008). An eddy-resolving hindcast simulation of the quasiglobal ocean from 1950 to 2003 on the Earth Simulator. In *High resolution numerical modelling of the atmosphere and ocean* (pp. 157–185). New York: Springer. https://doi.org/10.1007/978-0-387-49791-4_10

Sasaki, H., Sasai, Y., Kawahara, S., Furuichi, M., Araki, F., Ishida, A., et al. (2004). A series of eddy-resolving ocean simulations in the world ocean: OFES (OGCM for the Earth Simulator) project, OCEAN'04, 3, pp. 1535-14541.

Schiermeier, Q. (2013). Oceans under surveillance. *Nature*, *497*(7448), 167–168. https://doi.org/10.1038/497167a

Schmid, C. (2014). Mean vertical and horizontal structure of the subtropical circulation in the South Atlantic from three-dimensional observed velocity fields. *Deep Sea Research, Part I*, *91*, 50–71. https://doi.org/10.1016/j.dsr.2014.04.015

Schmid, C., Siedler, G. W., & Zenk, W. (2000). Dynamics of intermediate water circulation in the subtropical South Atlantic. *Journal of Physical Oceanography*, *30*(12), 3191–3211. https://doi.org/10.1175/1520-0485(2000)030<3191:DOIWCI>2.0.CO;2

Schott, F. A., Dengler, M., Zantopp, R., Stramma, L., Fischer, J., & Brandt, P. (2005). The shallow and deep western boundary circulation of the South Atlantic at 5°–11°S. *Journal of Physical Oceanography*, *35*(11), 2031–2053. https://doi.org/10.1175/JPO2813.1

Schouten, M. W., de Ruijter, W. P. M., van Leeuwen, P. J., & Lutjeharms, J. R. E. (2000). Translation, decay and splitting of Agulhas rings in the southeastern Atlantic Ocean. *Journal of Geophysical Research*, *105*(C9), 21,913–21,925. https://doi.org/10.1029/1999JC000046

Schumann, E. H., & Brink, K. H. (1990). Coastal-trapped waves off the coast of South Africa: Generation, propagation and current structures. *Journal of Physical Oceanography*, *20*(8), 1206–1218. https://doi.org/10.1175/1520-0485(1990)020<1206:CTWOTC>2.0.CO;2

Shannon, L. V., & Nelson, G. (1996). The Benguela: Large scale features and processes and system variability. In *The South Atlantic* (pp. 163–210). Berlin, Heidelberg: Springer.

Shillington, F. A., Reason, C. J. C., Rae, C. D., Florenchie, P., & Penven, P. (2006). 4 large scale physical variability of the Benguela Current Large Marine Ecosystem (BCLME). *Large Marine Ecosystems, Elsevier*, *14*, 49–70. https://doi.org/10.1016/S1570-0461(06)80009-1

Sloyan, B. M., & Rintoul, S. R. (2001). Circulation, renewal, and modification of Antarctic mode and intermediate water. *Journal of Physical Oceanography*, *31*(4), 1005–1030. https://doi.org/10.1175/1520-0485(2001)031<1005:CRAMOA>2.0.CO;2

Smith, W. H., & Sandwell, D. T. (1997). Global sea floor topography from satellite altimetry and ship depth soundings. *Science*, *277*(5334), 1956–1962. https://doi.org/10.1126/science.277.5334.1956

Speer, K., Siedler, G., & Talley, L. D. (1995). The Namib Col current. *Deep Sea Research, Part I*, *42*(11-12), 1933–1950. https://doi.org/10.1016/0967-0637(95)00088-7

Speich, S., Blanke, B., & Cai, W. (2007). Atlantic meridional overturning circulation and the Southern Hemisphere supergyre. *Geophysical Research Letters*, *34*, L23614. https://doi.org/10.1029/2007GL031583

Speich, S., Arhan, M., Ansorge, I., Boebel, O., Sokov, A., Gladyshev, S., et al. (2007). GOODHOPE/Southern Ocean: A study and monitoring of the Indotlantic connections. *Mercator Newsletter*, *2007*(27), 29–41.

Stommel, H. (1957). A survey of ocean current theory. *Deep Sea Research*, *4*, 149–184. https://doi.org/10.1016/0146-6313(56)90048-X

Stramma, L., & England, M. (1999). On the water masses and mean circulation of the South Atlantic Ocean. *Journal of Geophysical Research*, *104*(C9), 20,863–20,883. https://doi.org/10.1029/1999JC900139

Stramma, L., & Peterson, R. G. (1989). Geostrophic transport in the Benguela current region. *Journal of Physical Oceanography*, *19*(10), 1440–1448. https://doi.org/10.1175/1520-0485(1989)019<1440:GTITBC>2.0.CO;2

Talley, L. D. (2003). Shallow, intermediate, and deep overturning components of the global heat budget. *Journal of Physical Oceanography*, *33*(3), 530–560. https://doi.org/10.1175/1520-0485(2003)033<0530:SIADOC>2.0.CO;2

Thomson, R. E., & Emery, W. J. (2014). *Data analysis methods in physical oceanography* (3rd ed., p. 728). Newnes: Elsevier Science.

Valentine, H. R., Lutjeharms, J. R. E., & Brundrit, G. B. (1993). The water masses and volumetry of the southern Agulhas current region. Deep Sea Res. *Part I*, *40*(6), 1285–1305. https://doi.org/10.1016/0967-0637(93)90138-S

Valla, D., Piola, A. R., Meinen, C. S., & Campos, E. (2018). Strong mixing and recirculation in the northwestern Argentine Basin. *Journal of Geophysical Research: Ocean*, *123*(7), 4624–4648. https://doi.org/10.1029/2018JC013907

van Aken, H. M., Van Veldhoven, A. K., Veth, C., De Ruijter, W. P. M., Van Leeuwen, P. J., Drijfhout, S. S., et al. (2003). Observations of a young Agulhas ring, Astrid, during MARE in March 2000. *Deep Sea Research, Part II*, *50*(1), 167–195. https://doi.org/10.1016/S0967-0645(02)00383-1

van Sebille, E., England, M. H., & Froyland, G. (2012). Origin, dynamics and evolution of ocean garbage patches from observed surface drifters. *Environmental Research Letters*, *7*(4), 044040. https://doi.org/10.1088/1748-9326/7/4/044040

Veitch, J., Hermes, J., Lamont, T., Penven, P., & Dufois, F. (2017). Shelf-edge jet currents in the Southern Benguela: A modelling approach. *Journal of Marine Systems*, *188*, 27–38. https://doi.org/10.1016/j.jmarsys.2017.09.003

Veitch, J., Penven, P., & Shillington, F. (2010). Modeling equilibrium dynamics of the Benguela current system. *Journal of Physical Oceanography*, *40*(9), 1942–1964. https://doi.org/10.1175/2010JPO4382.1

Veitch, J. A., & Penven, P. (2017). The role of the Agulhas in the Benguela current system: A numerical modeling approach. *Journal of Geophysical Research: Ocean*, *122*, 3375–3393. https://doi.org/10.1002/2016JC012247

Watts, D. R., & Johns, W. E. (1982). Gulf stream meanders: Observations on propagation and growth. *Journal of Geophysical Research*, *87*(C12), 9467–9476. https://doi.org/10.1029/JC087iC12p09467

Watts, D. R., & Kontoyiannis, H. (1990). Deep-ocean bottom pressure measurement: Drift removal and performance. *Journal of Atmospheric and Oceanic Technology*, *7*(2), 296–306. https://doi.org/10.1175/1520-0426(1990)007<0296:DOBPMD>2.0.CO;2

Watts, D. R., & Rossby, H. T. (1977). Measuring dynamic heights with inverted echo sounders: Results from MODE. *Journal of Physical Oceanography*, *7*(3), 345–358. https://doi.org/10.1175/1520-0485(1977)007<0345:MDHWIE>2.0.CO;2

Watts, D. R., Sun, C., & Rintoul, S. (2001). A two-dimensional gravest empirical mode determined from hydrographic observations in the Subantarctic Front. *Journal of Physical Oceanography*, *31*(8), 2186–2209. https://doi.org/10.1175/1520-0485(2001)031<2186:ATDGEM>2.0.CO;2

Watts, D. R., Tracey, K. L., Bane, J. M., & Shay, T. J. (1995). Gulf stream path and thermocline structure near 74°W and 68°W. *Journal of Geophysical Research*, *100*(C9), 18,291–18,312. https://doi.org/10.1029/95JC01850

Weijer, W., de Ruijter, W. P., Dijkstra, H. A., & Van Leeuwen, P. J. (1999). Impact of interbasin exchange on the Atlantic overturning circulation. *Journal of Physical Oceanography*, *29*(9), 2266–2284. https://doi.org/10.1175/1520-0485(1999)029<2266:IOIEOT>2.0.CO;2

Weijer, W., & van Sebille, E. (2014). Impact of Agulhas leakage on the Atlantic overturning circulation in the CCSM4. *Journal of Climate*, *27*(1), 101–110. https://doi.org/10.1175/JCLI-D-12-00714.1

Whittle, C., Lutjeharms, J. R. E., Rae, D., & Shillington, F. A. (2008). Interaction of Agulhas filaments with mesoscale turbulence: A case study. *South African Journal of Science*, *104*(3–4), 135–139.